Journal International of Modern Engineering
WWW.IJME.US
Print ISSN: 2157-8052
Online ISSN: 1930-6628

INTERNATIONAL JOURNAL OF MODERN ENGINEERING

Spring/Summer 2023
Volume 23, No. 2

The Leading Journal of Engineering, Applied Science and Technology

Industrial
Electronics
Biomedical
Civil
Aerospace
Computer

Electrical
Chemical
Mechanical

ENGINEERING

THE LEADING JOURNAL OF ENGINEERING, APPLIED SCIENCE, AND TECHNOLOGY

Print ISSN: 2157-8052
Online ISSN: 1930-6628

www.ijme.us

www.iajc.org

INTERNATIONAL JOURNAL OF MODERN ENGINEERING

ABOUT IJME:

- IJME was established in 2000 and is the first and official flagship journal of the International Association of Journal and Conferences (IAJC).
- IJME is a high-quality, independent journal steered by a distinguished board of directors and supported by an international review board representing many well-known universities, colleges and corporations in the U.S. and abroad.
- IJME has an impact factor of **3.00**, placing it among the top 100 engineering journals worldwide, and is the #1 visited engineering journal website (according to the National Science Digital Library).

OTHER IAJC JOURNALS:

- The International Journal of Engineering Research and Innovation (IJERI)
  For more information visit www.ijeri.org
- The Technology Interface International Journal (TIIJ).
  For more information visit www.tiij.org

IJME SUBMISSIONS:

- Manuscripts should be sent electronically to the manuscript editor, Dr. Philip Weinsier, at philipw@bgsu.edu.

  For submission guidelines visit
  www.ijme.us/submissions

TO JOIN THE REVIEW BOARD:

- Contact the chair of the International Review Board, Dr. Philip Weinsier, at philipw@bgsu.edu.

  For more information visit
  www.ijme.us/ijme_editorial.htm

INDEXING ORGANIZATIONS:

- IJME is currently indexed by 22 agencies. For a complete listing, please visit us at www.ijme.us.

Contact us:

Mark Rajai, Ph.D.

Editor-in-Chief
California State University-Northridge
College of Engineering and Computer Science
Room: JD 4510
Northridge, CA 91330
Office: (818) 677-5003
Email: mrajai@csun.edu

www.tiij.org

www.ijeri.org

INTERNATIONAL JOURNAL OF MODERN ENGINEERING

The INTERNATIONAL JOURNAL OF MODERN ENGINEERING (IJME) is an independent, not-for-profit publication, which aims to provide the engineering community with a resource and forum for scholarly expression and reflection.

IJME is published twice annually (fall and spring issues) and includes peer-reviewed articles, book and software reviews, editorials, and commentary that contribute to our understanding of the issues, problems, and research associated with engineering and related fields. The journal encourages the submission of manuscripts from private, public, and academic sectors. The views expressed are those of the authors and do not necessarily reflect the opinions of the IJME editors.

EDITORIAL OFFICE:

Mark Rajai, Ph.D.
Editor-in-Chief
Office: (818) 677-2167
Email: ijmeeditor@iajc.org
Dept. of Manufacturing Systems Engineering & Management
California State University-Northridge
18111Nordhoff Street
Northridge, CA 91330-8332

THE INTERNATIONAL JOURNAL OF MODERN ENGINEERING EDITORS

TABLE OF CONTENTS

Editor's Note: Electric Vehicles and Regenerative Braking *3*
Philip Weinsier, IJME Manuscript Editor

Design of a Vertical Stirred Ball Mill to Produce Flaky Metal Powder..... *5*
A.H.M.E. Rahman, Pennsylvania State University – Harrisburg;
Issam-Abu Mahfouz, Pennsylvania State University – Harrisburg;
Anil Attaluri, Pennsylvania State University – Harrisburg

Modeling of Passenger Postures for Predicting Driving Events using a Support Vector Machine *11*
Mohammad Y. M. Naser, Kennesaw State University;
Sylvia Bhattacharya, Kennesaw State University;
Khalil M. Alame, Kennesaw State University;
Hairston, William David, US Army Research Lab, Baltimore City Council, Maryland

Modeling and Control of Regenerative Braking in a Multi-mode Plug-in Hybrid Electric Vehicle..... *17*
Aneesh Suri, Kettering University; Diane L. Peters, Kettering University

Review of Surrogate Safety Measures for Roadway Safety Analysis..... *28*
Nathaniel Edelmann, Boise State University; Mandar Khanal, Boise State University

Instructions for Authors: Manuscript Formatting Requirements *40*

In This Issue (p.17)
Electric Vehicles and Regenerative Braking

Philip Weinsier, IJME Manuscript Editor

Internal combustion engines and electric vehicles differ in one major way: regenerative braking. Regenerative braking is when the electric motor slows the vehicle via electromagnetism when the motor is operated in reverse, thereby capturing some of the kinetic energy that is used to charge the battery. This action occurs automatically when, for example, we take our foot off the accelerator or press lightly on the brake pedal. Slowing the vehicle in this way reduces wear on the brakes, thereby extending the life of the brake pads and/or discs. Not all regenerative braking systems are created equally. Different makes and models can not only have differing systems but also different levels of braking.

The U.S. Department of Energy gives us the following information on energy requirements for electric vehicles—in this case, the numbers represent the requirements for combined city/highway driving.

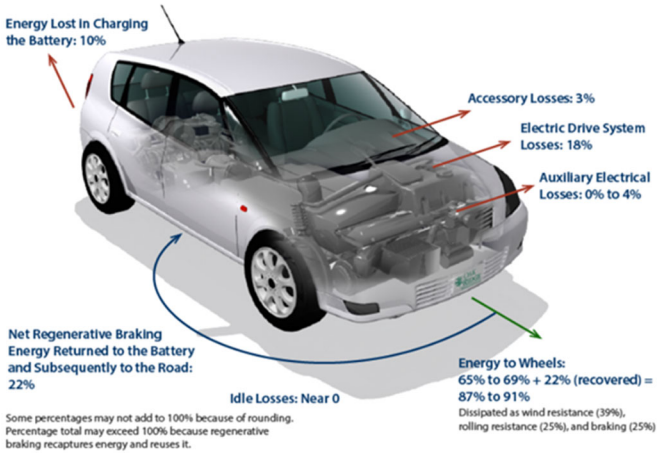

Of note is the energy lost in charging the battery (10%). Here, during charging, energy is lost in converting AC current from the electrical grid to DC current for use in the battery, as well as in overcoming the battery's resistance to charging. For the electric drive system losses (18%) of electric cars are much more efficient than the engines and transmissions of conventional vehicles, though some of the vehicle's energy is lost through drivetrain inefficiencies. With regards to the energy to the wheels, braking losses occur as lost heat through friction at the brakes when engaged, such that energy is initially used to overcome inertia and propel the vehicle.

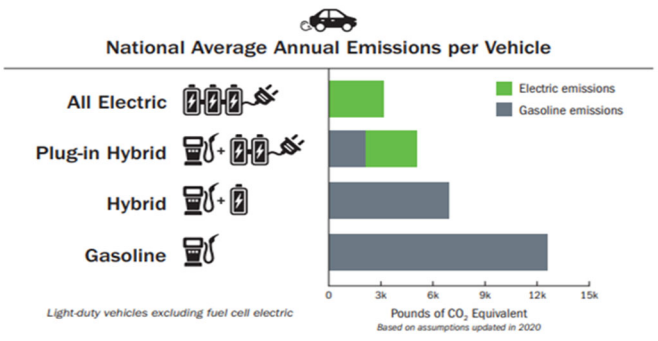

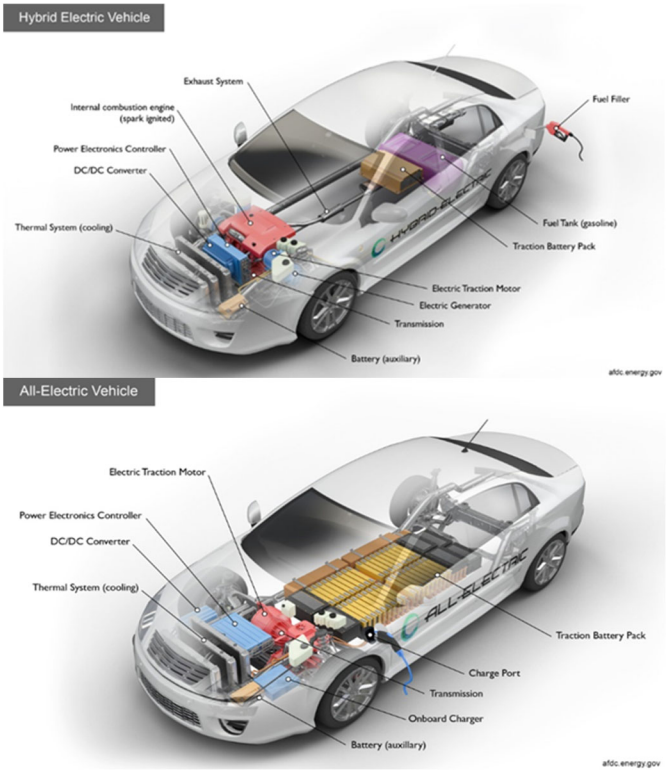

Electric cars use regenerative braking to recover some energy that would otherwise be lost in braking. Aerodynamic drag also causes a vehicle to expend energy in order to move air out of the way as it goes down the road—less energy at lower speeds and more as speed increases. This resistance is directly related to the vehicle's shape and frontal area. Rolling resistance is a resistive force caused by the deformation of a tire as it rolls on a flat surface. For cars, a 5%–7% reduction in rolling resistance increases fuel efficiency by 1%, but these improvements must be balanced against traction, durability, and noise.
[U.S. Department of Energy, www.fueleconomy.gov]

In the study featured here (p.17), the authors designed parallel regenerative braking systems to test for optimum stopping distance and energy conserved while braking. The results can be used to design better braking algorithms based on particular vehicles and their uses.

Editorial Review Board Members

Design of a Vertical Stirred Ball Mill to Produce Flaky Metal Powder

A.H.M.E. Rahman, Pennsylvania State University – Harrisburg; Issam-Abu Mahfouz, Pennsylvania State University – Harrisburg; Anil Attaluri, Pennsylvania State University – Harrisburg

Abstract

Flaky metal powder provides the maximum contact area with carbon nanotube (CNT) reinforcements in CNT-reinforced metal matrix composites. The vertical stirred ball (VTB) mill turned out to be effective in the production of flaky metal powder. In this current project, the authors designed and tested a vertical stirred portable ball mill add-on using a computer numerically controlled (CNC) mill to produce flaky powder from spherical powder. The VTB mill consisted of a jar and stirring method constructed primarily of 304 stainless steel. The mill had total volume capacity of around one liter and was tested using the 304 stainless-steel grinding balls in a liquid medium containing aluminum powder. The stirring speed was controlled using the CNC mill, and thus limited by the mill's capacity. Analysis using a scanning electron microscope (SCM) revealed that the vertical stirred ball mill provided the necessary attrition action to produce flaky powder. The starting spherical powder average diameter was 15 μm. After four hours of milling, the particles transformed into a flaky shape with an average thickness of 1 μm.

Introduction

Comminution is the oldest technology for reducing particle size. The energy efficiency of comminution is very low and requires more energy as the final particle size decreases. Grinding can reduce particle size, grow particle size, and create mechanical alloying. It also disintegrates, deforms, or cold welds the impacted particles. Grinding can produce polymorphic transformation as well (Senna & Kuno, 1971). During the grinding process, the disruption of a particle happens through several phases—localized concentrations of strains, formation of embryonic microcracks, formation of critical cracks by joining embryonic micro cracks, and, finally, disruption into several small particles. During the grinding process, the particles get trapped in between two colliding media (balls). This process is typically observed in tumbling, vibratory, and attrition ball milling for both dry and wet milling conditions.

Carbon nanotubes (CNTs) are getting attention as a reinforcement in aluminum matrix composites (AMCs), because of their superior mechanical properties (Singla, Amulya & Murtaza, 2015). However, there are some bottlenecks. One of the issues is the adhesion of CNTs to spherical aluminum (Al) powders. Adhesion is limited by spherical Al powders and creates a curvature effect, due to the morphological mismatch between CNTs and Al powder particles (Jiang, Li, Fan, Cao & Zhang, 2012). The size incompatibilities can be overcome by introducing flake-shaped powder particles. The flaky powder increases contact area to a great extent, thereby reducing the curvature effect. Therefore, flake-shaped Al powders are commonly used to prepare CNT-reinforced AMCs.

In the grinding process, breakage is the dominant mode of attrition, where particles are fragmented due to the stress acting on a particle in between two grinding balls. The most important parameter is the stress intensity, which determines the milling efficiency. There is another effect from the gravitation on the stress intensity for vertical stirred mills. In this paper, the authors discuss the design of a batch vertical mill add-on to a CNC mill in order to convert spherical powders to flake-shaped powder. The stirrer, mill jar, and connection to the CNC spindle were designed and the unit was tested and validated for performance.

Grinding Equipment and Techniques

(Neikov, 2009)

During the grinding process, grinding energy is transferred to the materials via grinding media, which can be balls, pebbles, or rods. Based on the motion, the ball mill can be classified as tumbling ball mills, vibration mills, or planetary mills. Tumbling ball mills are most widely used and operated continuously or in a batch, both in wet and dry conditions. The charge can be small or large and the critical speed (rpm) can be calculated using Equation 1:

$$n = \frac{42.3}{\sqrt{D_m}} \tag{1}$$

where, D_m is the mill diameter in meters.

The rotation should be set at 65-80% of the critical speed to avoid any centrifugation of balls to the wall. It should be noted that these data are approximate and may need to be adjusted for specific applications, as metal particles tend to agglomerate. The size of the grinding media was calculated using Equation 2:

$$d_{b.\min} = 10 d_{b.\max} \sqrt[3]{\frac{\sigma^2}{0.128 E \rho_b D}} \tag{2}$$

where, $d_{b.\min}$ is the minimum diameter of the ball (mm), $d_{b.\max}$ is the maximum size of feed (mm), σ is the compression strength (MPa), E is elastic modulus (MPa), ρ_b is the density of material of balls (kg/m^3), and D is the inner diameter of the mill body (m).

The advantages include universality and ease of operation. The shortcomings include large weight, high energy consumption, and noise. In a vibratory ball mill, the motion of the media is oscillatory. The motions of the media and particles are determined by several factors such as speed, amplitude, and curvature of the mill chamber side walls. The balls move around the wall and horizontally in a spiral trajectory causing substantial shearing action, which is desirable in mixing processes. The vibratory ball mill can produce an excellent soli state and dispersion-strengthened alloys. The optimum milling condition is achieved at a ball fill of 60-70% of the volume for a tube with a diameter of 5m.

A planetary mill consists of a revolving base disk and rotating mill pots. The rotation of the base is in the opposite direction of the mill pots. The centrifugal force generated in this case is enormous and the acceleration can get as high as 150 times that of the earth's gravity, *g*. Planetary ball mills are used in batch operations and, more often than not, for research applications. Grinding media and jars are available in different materials: silicon nitride, sintered corundum, zirconia, chrome steel, chrome–nickel steel, tungsten carbide, agate, and plastic polyamide.

The stirred mill has been proven to be very effective and is being integrated into traditional grinding circuits. These mills are attractive because their energy consumption is 30-40% less than conventional ball mills. The stirred mills can be broadly classified as vertical stirred mills and horizontal mills. The stirrer shapes are either a helical screw, a pinned shaft, or a disc. The rotation of the stirrer lifts the media charge in the center of the mill and then descends along the outside of the screw. It creates a violent centrifugal action on the grinding media and the slurry and promotes the lifting and propelling of the contents through the mill. The kinetic energy generated produces the energy needed for abrasion of fine particles and helps reduce overall size.

CNC Add-on Vertical Stirred Mill Design

The primary constraint for the proposed design of the mill was the height. The height was limited by the vertical space available between the CNC mill table and the spindle (tool holder). Another constraint imposed was the cost. The entire system was budgeted under $500. The system also had to be able to be fixed onto the table of the milling machine in a repeatable way and provide enough clearance between the tool and the unit for the operator to change tools and perform referencing cycles. The primary use of this mill was decided to be Al powder and in a wet mill condition. The stirring method design specifications focused on the function and installation process. For these solution criteria, metrics for clearance, hardness, operating speed, and installation time were established. Clearance was one of the most important specifications for this design. In vertical stirred ball mills, "dead zones" are created by inactivity at the inside surface and bottom of the jar, so for this current design, the authors aimed to get as close to the bottom and sides of the jar as possible (Daraio, Villoria, Ingram, Alexiadis, Stitt & Marigo, 2020). There are two options for clearance related to the size of the grinding balls. The stirring system either must be a minimum of one diameter of the grinding balls or a maximum of one radius of the grinding balls away from any jar surface. If the distance from the stirrer to the jar is between the radius and diameter of the grinding balls, then the ball can get lodged between the stirrer and jar and cause catastrophic failure. The preferred distance is less than one radius to avoid dead spots, thereby completely ensuring that no grinding balls or, therefore, powder collects at the surface of the jar. However, dangers can arise if there is significant wear in the jar or on the stirrer.

Figure 1 shows jar design and stirrer and mill adopter with exploded views without screws and welds. The components were pre-built and bought from vendors. The assembly was completed using welding and screws. The stacked bearings shown here consist of the flanged ball bearing, which sits in the lid and keeps the stirrer aligned, and the three-piece thrust roller pin bearing, which keeps the stirrer from falling deeper than intended into the jar. The top component is a set-screw collar that attaches to the shaft of the stirrer and rests on the top thrust bearing washer providing axial support. This collar can easily be adjusted to meet clearance specifications, removed to swap stirring methods, or replaced due to wear. The blades were connected to the shaft using ¼ - 20 screw. The adopters were purchased from vendors and cut to the desired lengths.

The position of the top blade of the stirrer was placed closer to the bottom. This change caused more necessary action in the mill and was easier to machine. A standard ¼"-20 central screw was used as the method of fastening the different pieces of the stirrer together. This provided an easy method for centering the pieces of the stirrer and eliminated the need for relying on welding or epoxy for critical stress points. This design also allowed for adjustments and modifications. After the stirrer was screwed together, epoxy was used to seal the gaps between parts and to keep the parts from unscrewing for any reason. The entire bearing assembly and mill-to-stirrer adapter were standard parts. The deep socket in the middle of the model is transparent to show its torque transferring female components. The top of the stirrer shaft was machined down to a hexagon such that the deep socket could sit on it. The top component was a sheared section of a socket extension to be used as the tool adapter. These components were inexpensive and allowed for the mill to breakaway safely from the unit if a malfunction should occur.

Figure 2 shows the optimized design of the stirrer, an exploded view of the assembly, and prints of different components. A threaded screw was used to assemble the stirrer shaft components and blades. The shaft was divided into

two parts. The lower part was 1" in length with internal thread. The screw held the two blades at the bottom and on the top of this part of shaft. The upper part of the shaft had an internal thread as well so that the screw could hold the lower part, the two blades, and the upper part together. Figure 2 also shows the standard top, front, and right-side views for each component.

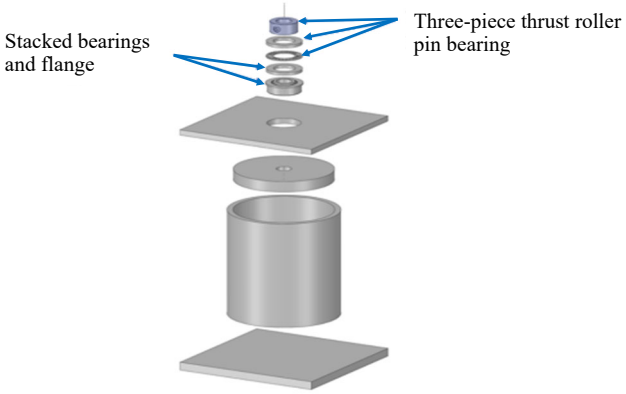

a) Exploded view of the jar assembly. (Screws and welds not included.)

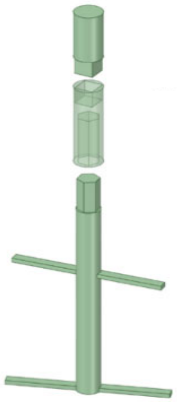

b) Exploded view of the stirrer and mill adapter.

Figure 1. Jar design.

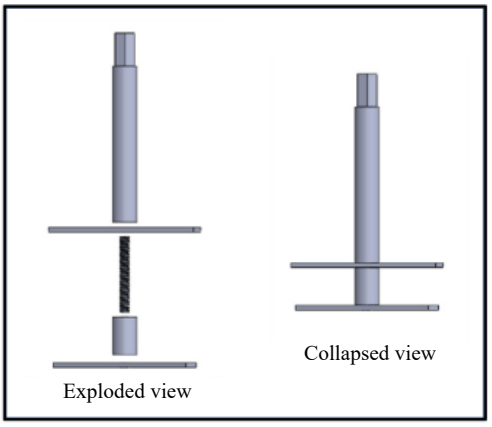

a) Optimized design and exploded view of the stirrer.

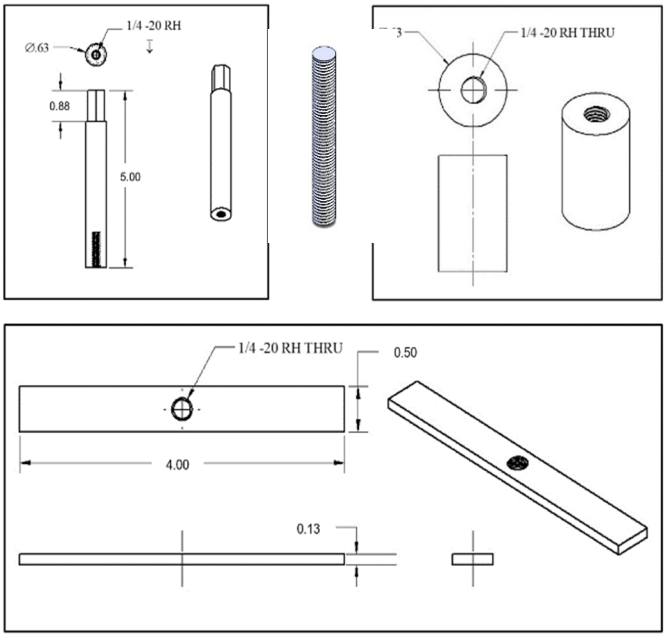

b) Prints of different components.

Figure 2. Different views of the stirrer.

Testing of the Completed Unit

Figure 3 shows how the final assembled unit was set on the HAAS mini mill. The figure also shows photos of the completed vertical stirred ball mill with a copper coil wrapping for cooling, secured to the mill table, lead opened and connected to the spindle of CNC mill. This setup was tested for a ball milling operation at 250 rpm. Table 1 shows the testing parameters. Aluminum powder with a size range of 10-14 micron spherical powder was used. Samples were collected during the cycle, which ensured a uniform sample. The samples were taken using a syringe about an inch or two down from the surface of the slurry and placed into small containers. The alcohol was then evaporated from the samples and the samples were analyzed using the SEM.

Figure 4 shows an example of the diameter measurement method for Sample 0 (control). In this control sample, the powder was clearly spherical. Average diameter was about 9.7 microns, which yielded an average volume of about 479 cubic microns and an average surface area of about 296 square microns. These measurements relatively match the labeled 10-14 micron size of the particles. The next sample was taken at one hour. Figure 5 shows an SEM image of Sample 1 after one hour of milling. The SEM image shows that an increasing flattening action occurred relatively uniformly. Average diameter increased to about 15.55 microns, which yielded an average thickness of about 3.8 microns and an increased average surface area of about 573 square microns using cylindrical property equations.

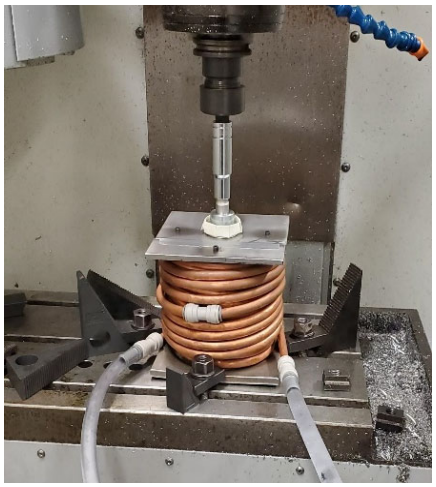

a) A completed unit with a copper coil wrapping for cooling.

b) The completed unit secured to the mill table.

c) The completed unit with the lead opened and connected to the spindle of CNC mill.

Figure 3. Testing of the completed unit.

Table 1. Prototype testing parameters.

Material	Mass (grams)
Aluminum Powder	65.9
Stainless Steel Balls	659
Isopropyl Alcohol	491.46
Stearic Acid	12.28
Total	1228.64

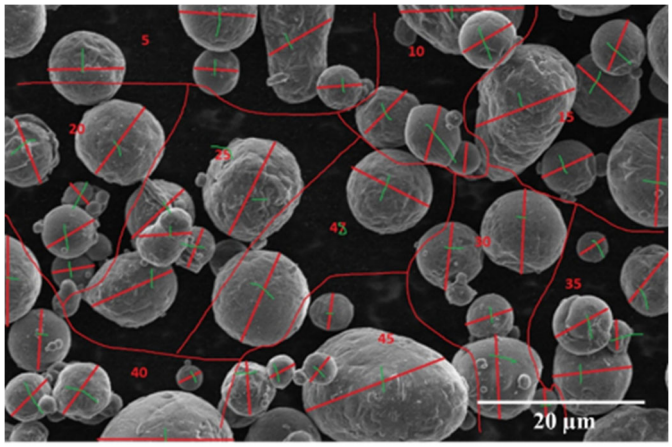

Figure 4. Example of diameter measurement method for Sample 0 (control).

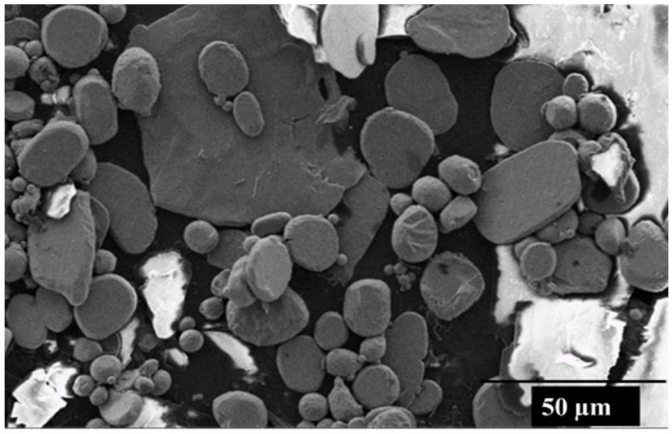

Figure 5. An SEM image of Sample 1 after one hour of milling.

Figure 6 shows an SEM image of Sample 2 after two hours of milling. After two hours of milling, the particles continued to flatten. It was difficult to determine the differences between the first and second hour; thus, the measurements reflected this similarity by showing a slight increase in both estimated surface area and thickness. Average diameter increased slightly to about 15.68 microns, along with average thickness to about 4.2 microns. However, average surface area increased only slightly to about 610 square microns.

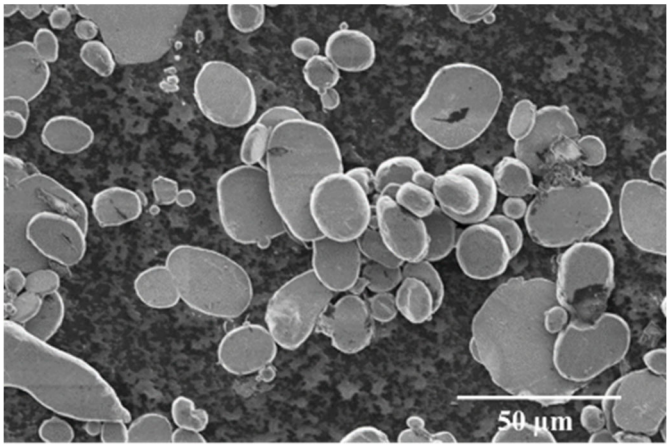

Figure 6. An SEM image of Sample 2 after two hours of milling.

Figure 7 shows an SEM image of Sample 4 after four hours of milling. While it was difficult to visually distinguish the measurements, calculations from the SEM image showed the greatest jump towards the desired results. Average diameter increased to about 27.2 microns. Estimated average thickness dropped to below 1.4 microns, or within 40% of the desired submicron thickness. Estimated average surface area increased by over 75% to about 1480 square microns.

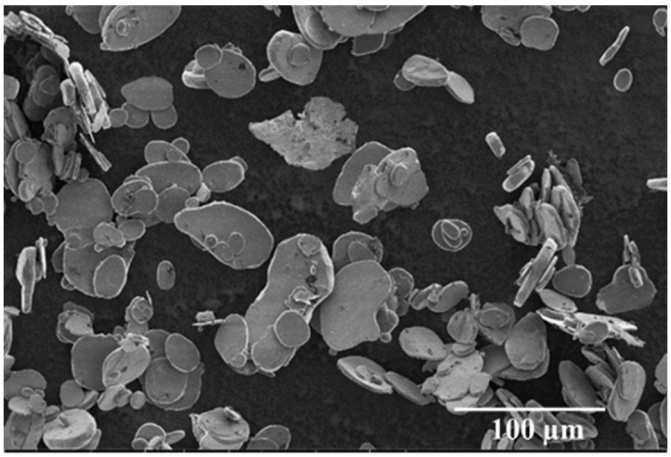

Figure 7. An SEM image of Sample 4 after four hours of milling.

Discussion

The mill principle was applied and worked as expected. The common principle was that the milling action would apply an attrition force on a particle in between two grinding media (balls) causing sever plastic deformation. Eventually, the particles fractured into smaller particles. However, the objective for this ball mill was to produce flaky-shaped powder. This newly designed ball mill was able to produce the desired results, although the milling parameters—such as milling time, rpm of the spindle, ball-powder ratio, etc.—needed to be optimized to obtain the desired particle sizes.

Conclusions

In this project, the authors built and tested the viability of vertical stirred ball mills to produce flaky aluminum powder from spherical aluminum powder for research in carbon nanotube-aluminum metal matrix composites. The ball mill's versatility was tested using a HAAS CNC mini-mill. The SCM analysis revealed that the vertical stirred ball mill provided the necessary action on the aluminum particles, increased surface area, and reduced width to near one micron on average. Even though the mill was able to produce flaky-shaped powder from a spherical shape, the flakes were not as thin as desired. However, the process parameters were not optimized. Moreover, the stirrer design needs to be improved.

Acknowledgments

This work was supported in part by the Multi-campus Research Experience for Undergraduate (MC-REU) at the University of Pennsylvania.

References

Daraio, F. D., Villoria, J., Ingram, A., Alexiadis, A., Stitt, E. H., & Marigo, M. (2020). Investigating grinding media dynamics inside a vertical stirred mill using the discrete element method: Effect of impeller arm length. *Powder Technology*, *364*, 1049-1061. https://doi.org/10.1016/j.powtec.2019.09.038

Jiang, L., Li, Z., Fan, G., Cao, L., & Zhang, D. (2012). The use of flake powder metallurgy to produce carbon nanotube (CNT)/aluminum composites with a homogenous CNT distribution. *Carbon, 50*, 1993-1998. https://doi.org/10.1016/j.carbon.2011.12.057

Neikov, O. D. (2009). Chapter 2: Mechanical Crushing and Grinding. In O. D. Neikov, S. S. Noboychenko, G. Dowson (Eds.), *Handbook of Nonferrous Metal Powders* (pp. 47-62). Elsevier.

Senna, M., & Kuno, H. (1971). Polymorphic transformation of PbO by isothermal wet ball-milling. *Journal of the American Ceramic Society*, *54*(5), 259-262. https://doi.org/10.1111/j.1151-2916.1971.tb12284.x

Singla, D., Amulya, K., & Murtaza, Q. (2015). CNT reinforced Aluminium matrix Composite-a review. Paper presented at the 4th International Conference on Materials Processing and Characterization. https://doi.org/10.1016/j.matpr.2015.07.248

Biographies

A.H.M.E. RAHMAN is an assistant professor of mechanical engineering at Pennsylvania State University – Harrisburg. He earned his BS from the University of Engineering and Technology of Bangladesh in 2004, and PhD in Mechanical Engineering in 2013 from the Universi-

ty of North Dakota. Dr. Rahman's research interests include light alloy technology, metal matrix composites, hybrid bio-composite, and diffusion bonding of specialty alloy. Dr. Rahman may be reached at aer15@psu.edu.edu

ISSAM ABU-MAHFOUZ is an associate professor of mechanical engineering at Pennsylvania State University – Harrisburg. He has taught courses in computer-aided design (CAD), finite element analysis (FEA), automatic controls, mechatronics, instrumentation, fluid power, design for manufacturability, dynamics, vibrations, optimization, energy systems, and smart systems. His research interests include machine condition monitoring, nonlinear vibrations, chaotic dynamics, machinery noise and vibration isolation, and the application of artificial intelligence to manufacturing processes. Dr. Abu Mahfouz continues to provide engineering consulting services in designing and developing new products, vibration and noise isolation, and machinery failure prevention. He is a licensed professional engineer. Dr. Abu-Mahfouz may be reached at iaa2@psu.edu

ANIL ATTALURI is an assistant professor of mechanical engineering at Pennsylvania State University – Harrisburg. His research goal is to cure cancer with cost-effective approaches that maintain a high quality of life. He develops novel devices and treatment planning systems for cancer treatments. Focusing on experimental, pre-clinical, and clinical validation, this work resulted in novel applicators and pioneering data for improving magnetic nanoparticle hyperthermia. Dr. Attaluri may be reached at aua473@psu.edu

Modeling of Passenger Postures for Predicting Driving Events using a Support Vector Machine

Mohammad Y. M. Naser, Kennesaw State University; Sylvia Bhattacharya, Kennesaw State University;
Khalil M. Alame, Kennesaw State University; Hairston, William David, US Army Research Lab, Baltimore City Council, Maryland

Abstract

Replacing human drivers with fully automated systems is the future of the vehicular system. Our role in a car will be as a passenger with little to no control over driving. However, current research is mostly driver-centered, and very little is known about the passenger. In this study, the authors investigated passenger posture in an attempt to understand their behavior during specific driving events. From this work, the authors present here a method for the analysis of passenger sitting postures and the resulting interactions of the passenger body with the car seat. First, pressure sensors were placed on the bottom and back of the passenger's seat for collecting the pressure values of the passenger when the car was moving. Second, a real road driving experiment was designed where the passenger and driver were engaged in normal conversation while data were being collected. During the drive, four driving events were recorded: lane change (both in right and left directions), aggressive acceleration, and braking. Passenger motion was used as a metric for predicting the four events via a support vector machine (SVM) classifier. In this study, the authors demonstrated the validity of the approach and how the team was able to achieve an average accuracy above 90% for five different drives carried out by different individuals.

Introduction

In the twenty-first century, both academia and modern industries have turned their interests to automated vehicle (AV) research. This field of research includes transportation systems, automotive engineering, human factors, information technology, control, robotics, communications, energy, security, and social sciences. While fully autonomous driving is the ultimate goal of automated vehicle research, intermediate highly automated vehicles, or HAVs, are fully capable technologies constructed for driving independently in most conditions. These HAVs are the stepping-stones to reaching fully automated vehicles and are expected to be commonplace in the vehicle industry in the next several years. This trend has been spurred by the Federal Automated Vehicles Policy introduced by the National Highway Traffic Safety Administration (NHTSA) of the United States in September, 2016 (U.S. Department of Transportation: NHTSA, 2016), which has taken a particular interest in these modes of transportation. According to the Society of Automotive Engineers (SAE), vehicles are divided into six levels, depending on who performs what and when. The levels are: 0 (no automation), 1 (driver assistance), 2 (partial automation), 3 (conditional automation), 4 (high automation), and 5 (full automation). According to ABI, it is expected to have eight million SAE level 3, 4, and 5 vehicles shipping by 2025 (ABI Research, 2018). Also, the National Association of Insurance Commissioners (NAIC) expects 3.5 million self-driving vehicles on U.S. roads by 2025 and 4.5 million by 2030 (National Association of Insurance Commissioners, 2022).

Consequently, the research on AVs is anticipated to continue expanding over time, with the goal of optimizing current designs in order to deliver the most optimal passenger experience. Conducting research on passenger behavior inside vehicles can provide valuable insights into the external environment of the vehicle, which can be used to develop improved driving algorithms and lead to enhanced safety, a more natural driving experience, and ultimately promote increased adoption of autonomous vehicles. The primary objective of this study was to investigate the correlation between passenger body posture and natural driving events performed by the driver. By examining these relationships, a deeper understanding of how passenger behavior can indicate driving events that can be realized while identifying opportunities for optimizing AV self-driving algorithms. However, this study only focused on passenger position, specifically identifying physical markers indicated by their sitting posture that would translate into specific driving behaviors. Despite passenger posture being relatively static, driving experience is highly dynamic, with external factors beyond the vehicle affecting driving behavior. To the best of the authors' knowledge, this paper represents the first attempt to conduct a comprehensive analysis of passenger posture, with the aim of obtaining insights that can inform the design of improved AVs.

Background

In the work, *Sitting Posture Monitoring System Based on a Low-Cost Load Cell Using Machine Learning* (Roh, Park, Lee, Hyeong, Kim & Lee, 2018), a sitting posture monitoring system (SPMS) was developed that used a combination of several sensors and machine learning classifiers to evaluate a sitting person's posture in real-time. Using a grid of four sensors for 24 healthy adult males and using support vector machines (SVMs) as classifiers, the authors reported average and maximum classification rates of 97.20% and 97.94%, respectively, in classifying six sitting postures. In the work, *A Sitting Posture Monitoring Instrument to Assess Different Levels of Cognitive Engagement* (Bibbo, Carli, Conforto & Battisti, 2019), eight sensors were used to examine the postures associated with four different leaning positions. The positions were then mapped in order to

exhibit a subject's cognitive engagement. The authors did not perform any testing; thus, no machine learning classifiers were used and no performance metrics were reported. In this current study, however, the authors showed a value in utilizing posture positions to infer some level of information on a test subject.

In the work, *Sitting Posture Analysis by Pressure Sensors* (Kamiya, Kudo, Nonaka & Toyama, 2008), a sensor sheet was developed to measure the pressure generated by a sitting person. Using the SVM classifier and 10 adult males, the authors were able to classify nine sitting postures with an accuracy of up to 93%. The only work known found that examined human posture in dynamic environments was by Ding, Suzuki, and Ogasawara (2017). Here, the driver's posture was estimated from the pressure distribution on the sensors. The authors used sensor sheets that each had 256 sensing cells on the chair. At first, the experiments were carried out via simulation, then evolved to road experiments. Using the SVM classifier for seven subjects, they achieved an average accuracy of 59% for the simulated experiments classifying eight different postures. Again, the focus of this current study was on analyzing the distribution of the driver's posture rather than that of the passenger, making the work presented in this paper the first of its kind in examining passenger posture data.

Methodology: Data Collection

The data for this study were gathered in a real-world driving scenario in 2016 by the U.S. Army Research Laboratory (ARL). A total of five drives were conducted, each by a different participant, and included both males and females. Each drive lasted approximately one to two hours, and covered a distance of around 24.5 miles, with the duration varying based on traffic conditions. The majority of the routes followed arterial roadways, with a few sections covering local roadways. Figure 1 illustrates how the passenger and vehicle were equipped with different types of sensors. In this paper, the authors focus on the sensors that were placed on the seats (not visible in the figure). These sensors captured valuable data on the passengers' postures and movements during the drives, forming the basis for the subsequent analysis. There were a total of 12 sensors used; Figure 2 shows the arrangement. Six sensors were placed on the backside of the seat (B1 through B6) and another six on the bottom of the seat (A1 through A6).

The distribution of the sensors was chosen to ensure maximum coverage of both the back and bottom surfaces of the seat without causing any discomfort to the participant. The sensors in the back (B1 through B6) will be referred to as Seat-Back sensors, and the other group (A1 through A6) will be referred to as Seat-Bottom sensors in this paper. The Seat-Back sensors were arranged with three rows of two sensors per row, while the Seat-Bottom sensors were arranged with two rows of three sensors per row.

Figure 1. Passenger (front seat) view during data collection.

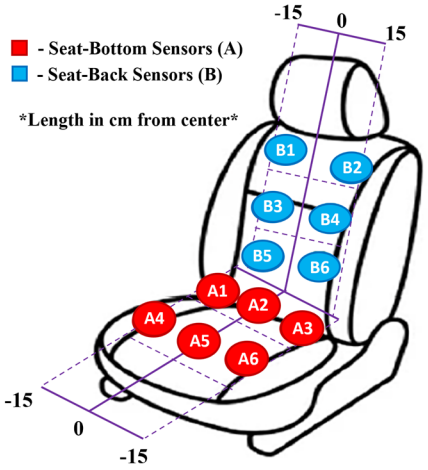

Figure 2. Distribution of pressure sensors.

Data Preprocessing

Before discussing the preprocessing step, a sample of the pressure values using Seat-Bottom and Seat-Back are projected in the graphs of Figures 3 and 4, respectively. Each color represents one of the sensors. The voltage on the y-axis is the output of the seat sensors, and is a linearly transformed version of the pressure detected. The data in Figure 3 show differences in the pressure values across the sensors with instances of overlapping, as one would expect. Figure 4 shows an atypical difference between the sensor values. For instance, sensors B5 and B6 on the Seat-Back should have similar values, as they are the same distance from the Seat-Bottom and are equidistant to the middle of the seat. However, both sensors showcase vastly different pressure values, as B6 provides little to no pressure values and B5 provides abnormally high pressure values. This pattern was observed in different drives and for different adjacent sensor pairs. Thus, the Seat-Back sensors were deemed corrupt, as the readings would lead to drawing invalid conclusions; only the Seat-Bottom sensors from Figure 4 were used in the analysis section.

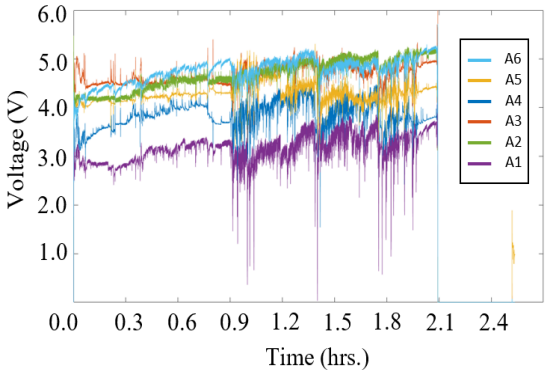

Figure 3. Seat-Bottom pressure sensor values for one of the drives.

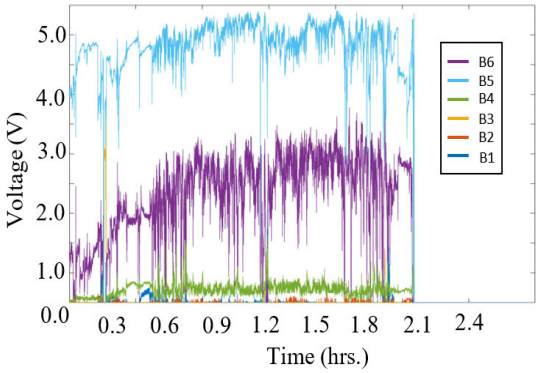

Figure 4. Seat-Back pressure sensor values for one of the drives.

While seated in a stationary position, specific parts of the body come into contact with sensors that detect changes in pressure values. These readings of the pressure distribution before the drive began were used as a baseline for a given subject. So, the data collected from the sensors throughout the drives were normalized based on the pre-drive pressure distribution. Regarding normalization of the data, real-time values for each sensor were subtracted from the initial values before the drive began. Regarding filtration of the data, no filtration was executed except for eliminating the specific Seat-Bottom sensors as just noted.

Driving Events

There were four driving events considered in this study. These events are listed as follows:

1. Switching Lanes to the Left: In the seconds leading up to a lane change, passengers may exhibit physical movements that anticipate the event. In particular, given that left lanes typically involve higher vehicle speeds, passengers may predict an upcoming lane change by observing other vehicles in close proximity to their own from the front side. It is important to note that this study specifically focused on event prediction, and therefore any movements made by the passenger in response to the actual lane change event did not impact the data used in classification.
2. Switching Lanes to the Right: The passenger may anticipate the need to switch lanes when they observe vehicles approaching their own from behind. In such situations, the driver will likely switch to the right lane to allow the faster vehicle to pass.
3. Braking: Braking is anticipated by the driver when the vehicle approaches slower-moving cars in front. This case is evident on both arterial roads and local roadways. Also, observing traffic lights or any other interaction on local roadways may subconsciously cause the passenger to react in a way that is reflected in their posture distribution.
4. Aggressive Acceleration: The passenger's position may also reflect acceleration, particularly in the case of aggressive acceleration, which often follows braking. Also, acceleration is a common occurrence on roadways, where drivers maintain a certain speed by periodically applying gas to the engine to keep the vehicle moving.

Now that the driving events have been defined, the use of the posture positions associated with the four occurrences may commence.

Classification

SVM is a powerful, supervised machine learning classifier that is widely implemented, due to its ability to learn well with a small number of parameters, its robustness against various model violations, and its computational efficiency compared to competing methods. The support vector relates to points that are closest to the hyperplane, while the margins correspond to the distance between the support vectors. Support vectors are data points that are closer to the hyperplane and influence the position and orientation of said hyperplane. The SVM kernel is a function that takes low-dimensional input space and imitates transforming it into a higher-dimensional space, mostly useful in non-binary classification problems. This is why the SVM classifier was chosen for this current study. The kernel used with the SVM was radial basis function (RBF), which is prevalent in machine learning applications of multi-class problems, similar to the one used here.

Results

The methodology employed in this study involved computing the average sensor readings over a 2-second period immediately preceding each recorded event. The sampling frequency was 10 samples per second, with a time window comprised of 20 samples. The length of the 2-second window was chosen after testing with varying window lengths, both greater and lesser than two seconds. Consequently, each event is characterized by six features, one for each sensor. Table 1 presents the event count for each of the five drives.

Table 1. Event counts for the five drives.

Subject	Driving Event			
	Braking	Aggressive Acceleration	Switching Lanes to the Left	Switching Lanes to the Right
S1	53	72	12	7
S2	56	97	27	26
S3	44	74	14	5
S4	48	422	7	8
S5	42	63	13	12

From this table, one can see that there is an imbalance in the number of events. Acceleration events were significantly higher than the others, which is particularly evident in S4. It is natural to observe more instances of acceleration events than braking events while driving, and this trend can be influenced by the driving style of the individual driving the vehicle. Data imbalance is a prevalent challenge while dealing with real-world data that are generated in uncontrolled environments. If no corrective measures are implemented, classifiers tend to learn less from the minority classes and become biased towards the majority class. Although there is no ideal solution for addressing this issue, some measures can help mitigate it. In this study, the classifier was trained on an up-sampled version of the data (UD) to match the highest number of events. Subsequently, to prevent overly optimistic results, the testing was performed on the original dataset (OD), as shown in Table 2.

Table 2. Data used for training and testing of Subject S2.

Dataset	Event Type							
	Braking		Aggressive Acceleration		Switching Lanes to the Left		Switching Lanes to the Right	
Event Count	OD	UD	OD	UD	OD	UD	OD	UD
	56	97	97	97	27	97	26	97

In this study, the original dataset was up-sampled to ensure that all event types had an equal number of instances, and a random 75% of these data were used for training the classifier. Testing the model on this up-sampled dataset could result in unrealistic and over-optimistic results. Therefore, to obtain more accurate results, five random 25% segments of the original dataset were used for testing the model. This process was repeated for each of the five drives conducted with different participants. Table 3 shows the accuracies achieved for the different splits for the five subjects. From this table, the average overall accuracy for all subjects is 93.52%, which is significantly higher than the chance level of 25% (4 classes). Individual accuracy averages for each participant ranged from 89.44% to 99.34%. These results provide evidence for the potential of using passenger posture data to infer information about vehicle driving.

Table 3. The accuracies achieved for the five drives using five random splits.

Subject	Accuracy for Split Percentage					
	1	2	3	4	5	Average
S1	91.67	91.67	91.67	83.33	88.89	89.44
S2	90.38	94.23	94.23	92.31	96.15	93.46
S3	94.29	91.43	94.29	97.14	80.00	91.43
S4	99.18	100.0	99.18	98.36	100.0	99.34
S5	96.97	96.97	96.97	84.85	93.94	93.94

Also, to ensure that all classes (events) are classified correctly and that those high accuracies are not driven by the majority event (acceleration), the confusion matrices corresponding to the highest split for the five subjects are shown in Figures 5-9. The y-axis in these matrices represents the true labels that the SVM classifier was designed to predict, while the x-axis shows the predicted labels generated by the model. The diagonal elements in the matrix represent the number of samples that were correctly classified for each event type. Ideally, a perfect prediction model would have no off-diagonal elements. However, this is very challenging to achieve in real-world scenarios. From the figures, it is clear that correctly classified events are evenly distributed between all event types, demonstrating the successful operation of the prediction model. This finding was also observed by examining the matrices generated for other splits as well.

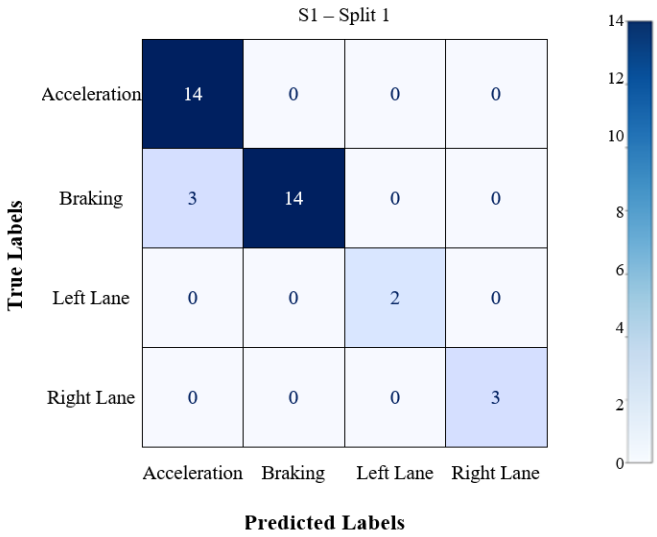

Figure 5. Confusion matrix split for S1.

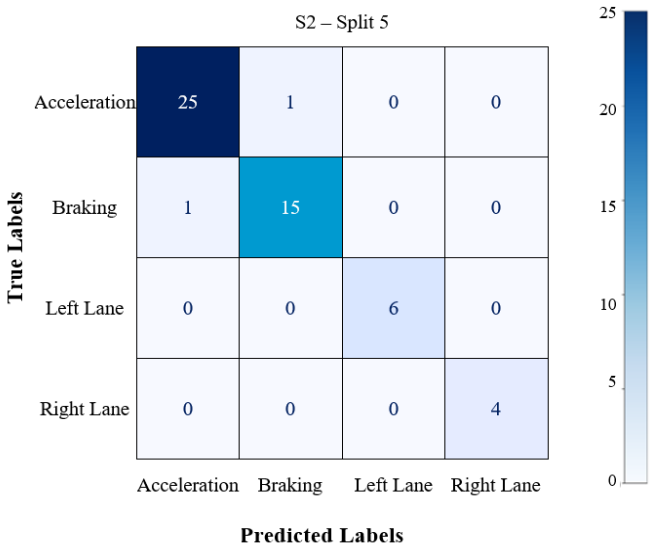

Figure 6. Confusion matrix split for S2.

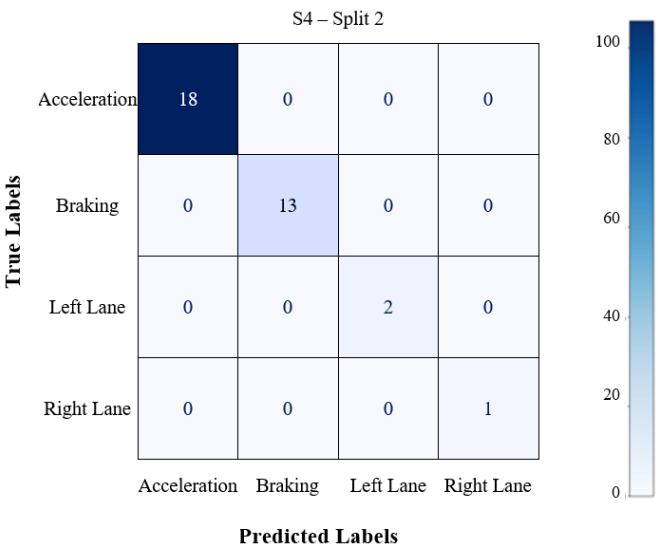

Figure 8. Confusion matrix split for S4.

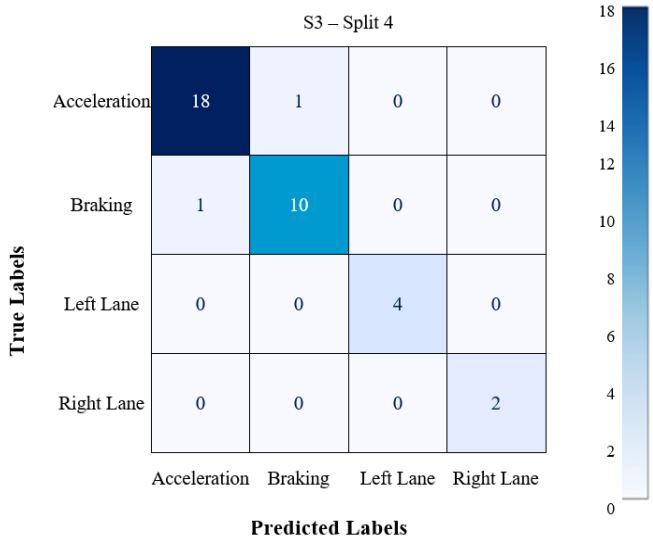

Figure 7. Confusion matrix split for S3.

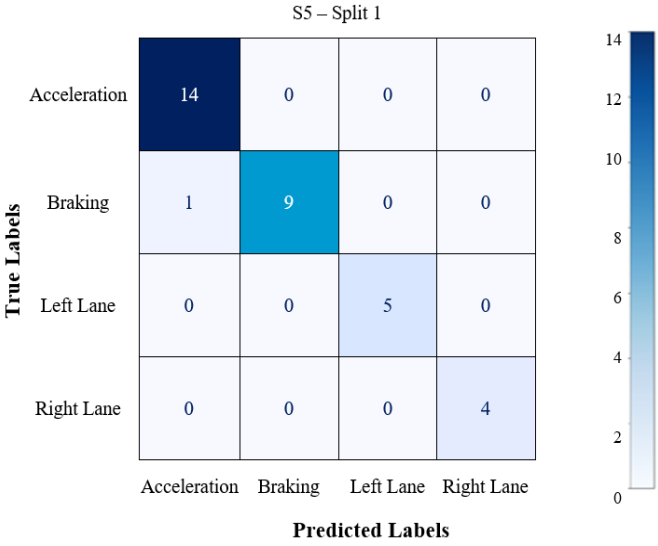

Figure 9. Confusion matrix split for S5.

Discussion

This study serves as a preliminary investigation into the potential of using passengers in a vehicle to provide valuable insights into driving behavior. Through the analysis of passenger posture data, collected from sensors placed on the bottom of the seat, this research was able to accurately classify four distinct driving events. These findings can have significant implications for the development of autonomous vehicle technology, as real-time feedback from passengers can be utilized to improve the driving algorithms of autonomous agents. As such, this study represents an important step towards the creation of more sophisticated autonomous vehicles that can adapt to the complex and dynamic nature of driving. That said, the paper is limited by the small dataset considered. Moreover, incorporating Seat-Back sensors in future research will enable the generation of heat maps to illustrate a passenger's real footprint for each event type.

Acknowledgments

The data that were used for this study were recorded under the auspices of the U.S. DEVCOM Army Research

Laboratory (ARL) Cognition and Neuroergonomics Collaborative Technology Alliance (Contract W911NF-10-2-0022; see more at https://www.arl.army.mil/cast/CaNCTA). The analyses described in this report are part of an ongoing collaborative effort that is supported in part by Kennesaw State University as well as funding from ARL's Human Autonomy Teaming Essential Research Program (Contract W911NF-2020205). The team would also like to both acknowledge and thank Dr. Jason Metcalfe (ARL) for valuable comments and guidance during the preparation of this manuscript.

References

ABI Research. (2018, April). ABI Research Forecasts 8 Million Vehicles to Ship with SAE Level 3, 4 and 5 Autonomous Technology in 2025. https://www.abiresearch.com/press/abi-research-forecasts-8-million-vehicles-ship-sae-level-3-4-and-5-autonomous-technology-2025/

Bibbo, D., Carli, M., Conforto, S., & Battisti, F. (2019). A Sitting Posture Monitoring Instrument to Assess Different Levels of Cognitive Engagement. *Sensors, 19*(3), 455. https://doi.org/10.3390/s19030455

Ding, M., Suzuki, T., & Ogasawara, T. (2017). *Estimation of driver's posture using pressure distribution sensors in driving simulator and on-road experiment*. Paper presented at the 2017 IEEE International Conference on Cyborg and Bionic Systems (pp. 215-220). https://doi.org/10.1109/CBS.2017.8266102

Kamiya, K., Kudo, M., Nonaka, H., & Toyama, J. (2008). *Sitting posture analysis by pressure sensors*. Paper presented at the 2008 19th International Conference on Pattern Recognition (pp. 1-4). https://doi.org/10.1109/ICPR.2008.4761863

National Association of Insurance Commissioners. (2022, December). Autonomous Vehicles. https://content.naic.org/cipr-topics/autonomous-vehicles

Roh, J., Park, H., Lee, K., Hyeong, J., Kim, S., & Lee, B. (2018). Sitting Posture Monitoring System Based on a Low-Cost Load Cell Using Machine Learning. *Sensors, 18*(2), 208. https://doi.org/10.3390/s18010208

U.S. Department of Transportation: NHTSA. (2016). Federal Automated Vehicles Policy: Accelerating the Next Revolution in Roadway Safety.

Biographies

MOHAMMAD Y. M. NASER received his BS in Electrical Engineering from the University of Jordan in 2018 and his MS in Renewable and Clean Energy Engineering (Mechanical Engineering) in 2021. Mr. Naser is a doctoral student at KSU majoring in interdisciplinary engineering with a focus on biomedical systems. His research interests include physiological signal processing, brain computer interaction (BCI), and multi-modal fusion (MMF). Mr. Naser may be reached at mnaser1@students.kennesaw.edu

SYLVIA BHATTACHARYA received her PhD in Electrical Engineering from Florida State University in 2019 and her MS in Applied Engineering from Georgia Southern University in 2016. Dr. Bhattacharya also has a background in biomedical engineering from the West Bengal University of Technology in India in 2013. She currently holds two positions: one as a Visiting Research Scientist at Google and the other as an assistant professor in the Department of Engineering Technology and Head of the Neuro-Interaction Innovation Lab at Kennesaw State University. Her research interests include neural signal processing, human-machine interaction, intelligent transportation system (ITS), prediction modeling using machine learning (ML), and data fusion modeling. Dr. Bhattacharya may be reached at sbhatta6@kennesaw.edu

KHALIL MICHAEL ALAME is studying electrical engineering at Kennesaw State University. Mr. Alame joined the Neuro-Interaction Innovation Lab in the spring of 2022. His research interests include analyzing electroencephalography (EEG) and acoustic holography. Mr. Alame may be reached at kalame@students.kennesaw.edu

WILLIAM DAVID HAIRSTON received his BS in Experimental Psychology from Appalachian State University in 1999, MS in Experimental Psychology from Wake Forest University in 2001, and his PhD in Neurobiology and Anatomy from the same institution in 2006. Since 2009, he has been working at the U.S. Army Research Laboratory, where he currently holds the position of Senior Principal Investigator. His research interests include multisensory integration, translational neuroscience, and sensor development. Dr. Hairston may be reached at william.d.hairston4.civ@army.mil

Modeling and Control of Regenerative Braking in a Multi-mode Plug-in Hybrid Electric Vehicle

Aneesh Suri, Kettering University; Diane L. Peters, Kettering University

Abstract

In this study, the authors used a systematic design methodology to design a regenerative braking system. The parallel brake systems were tested for their ability to deliver the optimum stopping distance and energy conserved while braking. The model of the vehicle was tested by using this regenerative system in a model of a flexible plug-in hybrid electric vehicle that was modeled for a multi-mode plug-in hybrid vehicle using MATLAB and Simulink. In addition to improving the overall efficiency of the vehicle, regenerative braking also extends the life of the brake pads, since the energy recapture process reduces the use of friction brakes. Implementing regenerative braking requires a control algorithm to determine the usage of both hydraulic brakes and regenerative brakes, and optimizing energy conservation during braking while ensuring the safety and stability of the vehicle by considering the dynamics of braking. The model created in this project was tested for different city driving cycles and integrated all components of a multi-mode hybrid electric vehicle and regenerative braking system to obtain maximum energy restoration out of each brake.

Introduction

The increase in demand by governing bodies to reduce vehicular exhaust and reduce fuel consumption has created a large interest in electric and hybrid vehicle technologies. Major auto manufacturers have their research teams invested in making new energy-efficient vehicles. The advantage of a hybrid electric vehicle (HEV) is that both the battery and the engine can run at optimum points, delivering maximum overall efficiency. The hybrid powertrain configurations can be classified into three types: parallel, series, and complex hybrid systems. A complex hybrid system provides the characteristic combination of both parallel hybrid and series. A highly coordinated energy management system is essential for having a flexible, operational powertrain such that it can perform the blending of torque, power, and speed from multiple power sources (Raut, Phalke & Peters, 2019).

The control system of the hybrid vehicle studied here featured multiple modes of operation with a wide range of possible combinations of fuel and battery usage. The modes were narrowed based on urban, suburban, and highway driving styles. The operation of the gasoline engine in urban driving stop-and-go conditions is inefficient; the electric powertrain is more efficient in these conditions (Ehsani, Gao, Longo & Ebrahimi, 2019). An additional advantage of an electric powertrain is that the energy consumed during braking can be recovered, stored, and used for propulsionpropulsion (Boerboom, 2012). Varying vehicle speeds in urban centers is highly dynamic; thus, braking consumes a significant amount of energy (Gao, Chen & Ehsani, 1999). To recover the energy that is typically lost as heat, regenerative braking is utilized. A regenerative braking system (RBS) minimizes energy loss and improves the fuel economy of the vehicle.

The energy that can be recovered through RBS is limited by the state of charge (SOC) and by braking torque requirements; if batteries are already at or near full charge, then no further energy can be stored. In addition, RBS cannot provide the full amount of braking torque that is required at times, and therefore the RBS has to be merged, or blended, with friction braking systems so that torque requirements can be met. The key criteria for brake blending are to provide proper braking force distribution in order to minimize braking distance stably and to recover the maximum possible amount of energy.

Configuration of the Multi-Mode Plug-in HEV

A hybrid vehicle platform provides an opportunity to reduce emissions and improve fuel economy by reducing transient losses, idling loss, and recapturing energy lost in braking. Traditional engines, during highway driving, perform more efficiently than in urban areas. At lesser loads (stop-and-go), traditional engines encounter higher levels of friction (Mechtenberg, 2009). By adding an electric motor to the traditional powertrain, the efficiency of lesser loads can be improved and braking energy lost to heat can be reduced by using the motor as a generator.

Many different hybrid configurations are able to utilize RBS systems; in this current study, the hybrid powertrain considered was first proposed by Mechtenberg (2009) and further developed by Mechtenberg and Peters (2012). Figure 1 shows the fundamental configuration of this front-wheel hybrid and Table 1 gives the values of the parameters for the vehicle. The powertrain system had a split fuel tank with a bi-fuel engine that could accommodate two different fuels in two different sets of engine cylinders (i.e., gasoline and compressed natural gas). To allow a greater degree of freedom with charging and discharging, the powertrain was equipped with two motors. One motor worked exclusively as a traction motor, while the other worked as both motor and generator. To facilitate both deep and shallow charging, two batteries were included in the system—one for the deep charging cycle while the vehicle is plugged in, and one for the shallow charging cycle (Raut et al, 2019).

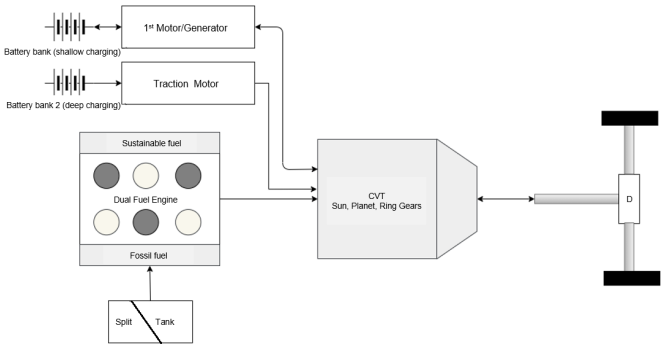

Figure 1. Schematic overview of the hybrid vehicle drivetrain configuration (Raut et al., 2019) (Mechtenberg & Peters, 2012).

Table 1. Parameters of the target hybrid electric vehicle (Raut et al., 2019).

Parameter	Value
Height	2 m
Width	2.5 m
Drag Coefficient	0.45
Gross Vehicle Mass	1900 kg
Height of Center of Gravity	0.6 m
Wheel Radius	0.35 m
Wheelbase	2.75 m

Brake Force Calculation

Based on the mode of braking selected, the model would calculate the total braking force. The braking dynamics changed based on the weight and load on the vehicle axle and the forces required to stop the vehicle change. The force to be generated by a braking system was calculated based on the vehicle dynamics and the behavior of the vehicle during braking (Breuer & Bill, 2008). Using the free-body diagram in Figure 2, the static forces on the vehicle were determined (Breuer & Bill, 2008). Several intermediate values were defined using Equations 1 and 2.

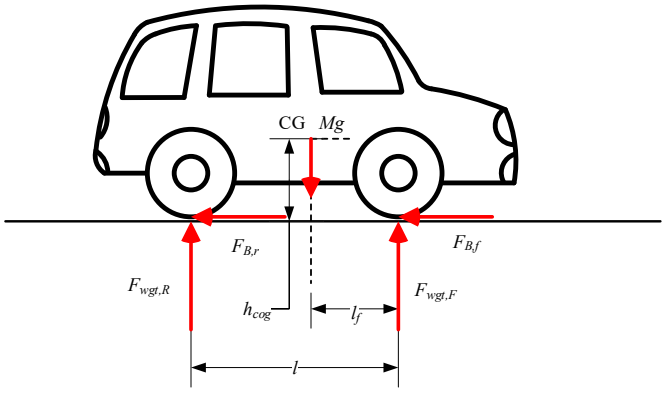

Figure 2. Forces acting on the vehicle while braking on level ground.

$$\Psi = \frac{F_{wgt,F}}{F_{weight}} = \frac{l_f}{l} \tag{1}$$

$$X = \frac{h_{CoG}}{l} \tag{2}$$

Newton's second law states that $F = ma$, where m is mass and a is acceleration. The deceleration, a/g of the vehicle is calculated from front and rear brake force proportions (Breuer & Bill, 2008). This leads to the relations given in Equations 3 and 4.

$$\frac{a}{g} F_{weight} = F_{wgt,F} + F_{wgt,R} \tag{3}$$

$$\frac{a}{g} = \frac{F_{wgt,F} + F_{wgt,R}}{F_{weight}} \tag{4}$$

In a braking maneuver, the dynamic axle load distribution is observed by using the principle of torque equilibrium around the center of tire contact of both the axles. The tire is the only point of contact between the road surface and the vehicle, leading to Equation 5:

$$FB = \mu_{x,B} F_{weight} \tag{5}$$

where, FB is the total braking force, $\mu_{x,B}$ is the coefficient of friction, and F_{weight} is considered as the normal force applied on the surface of the road.

This results in Equations 6 and 7. Similarly, Equation 8 can be used to find the forces on the rear axle.

$$F_{B,f} = \mu_{xBf} F_{wgt,F} \tag{6}$$

$$\frac{F_{B,f}}{F_{weight}} = \mu_{xBf} \frac{F_{wgt,F}}{F_{weight}} = \mu_{xBf} \left(1 - \Psi + \frac{a}{g} X\right) \tag{7}$$

$$\frac{F_{B,r}}{F_{weight}} = \mu_{xBr} \frac{F_{wgt,R}}{F_{weight}} = \mu_{xBr} \left(\Psi - \frac{a}{g} X\right) \tag{8}$$

The relationship between Equations 7 and 8 applies to the force transmission between tire and road as well. For a homogenous road, the friction coefficients are $\mu_{xBf} = \mu_{xBr}$ (Breuer & Bill, 2008).

Brake Blending

The total braking force demanded to decelerate is produced by braking at the front and rear axles. The amount of braking force to be applied on and shared between the front and rear axles is determined by brake blending.

Figure 3 shows that, with the rear braking force on the Y-axis and front braking force on the X-axis, the blending between the brakes is analyzed and referred to as the brake blending curve. The braking forces distribution is bounded by ECE regulation addendum 12 H: Regulation No. 13H (uniform provisions concerning the approval of passenger cars concerning to braking), which indicates that the front axle braking force under all conditions is to be higher than the rear axle braking force in order to ensure vehicle stability (Regulation No. 13-H-01: Passenger Car Braking, 2019). The minimum deceleration of the vehicle is given by Equation 9:

$$z \geq 0.1 + 0.85(k - 0.2) \tag{9}$$

where, z is the braking rate of the vehicle in g's and k is the theoretical coefficient of adhesion between tire and road (Regulation No. 13-H-01: Passenger Car Braking, 2019).

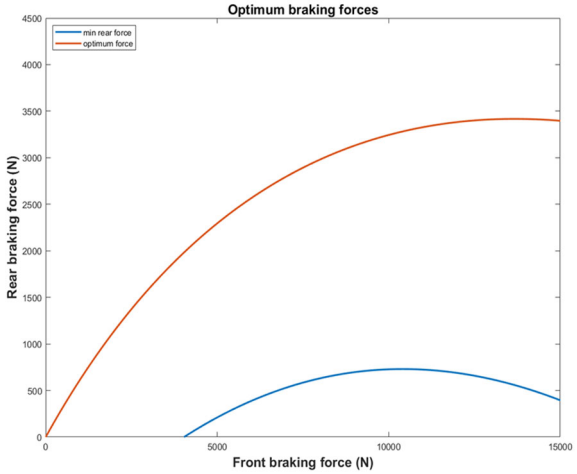

Figure 3. Optimum and minimum brake force distribution curve.

Given these rules, Figure 3 shows the optimum braking forces for both the front and rear brakes.

Regenerative Braking Configuration

The motor-generator converts the kinetic or potential energy of a vehicle's mass into electric energy that can be stored and reused. The plug-in HEV used in this current study was equipped with a series brake system. A series braking approach effectively recovers a significant amount of energy (Wang, Wu & Feng, 2019). Series braking uses a segmented distribution of regenerative braking and traditional braking power. The algorithm uses regenerative braking power after the braking demand reaches a certain value and then uses hydraulic braking. The front axle braking force is shared by regenerative and hydraulic brakes whereas the rear axle brake load is provided by hydraulic brakes. Figure 4 shows a schematic of the series braking scheme. The braking forces on the front and rear axles are distributed according to the regulations stated in ECE Regulations 13H (Regulation No. 13-H-01, 2019). The designed control algorithm should deliver a braking force such that the braking force on the front and rear axles are nearly equal to the optimum/ideal braking force. The optimum/ideal brake force distribution would ensure the stability of the car and that it would stop in the shortest distance.

Modeling of a Multi-Mode Plug-in Hybrid Electric Vehicle

The multi-mode plug-in HEV model was based on the model by Raut et al. (2019). The vehicle model for this HEV was structured as a collection of subsystems, where each subsystem had a specified function in the overall vehicle. Figure 5 shows the subsystems, which were based on functionality—driver, drive-mode controller, engine, electrical systems, driveline, vehicle dynamics, and braking systems. In the driver model, the actual vehicle speed was compared to the target speed input from the drive cycle. The difference in speeds (error) was provided as input to a PI controller, which was tuned to minimize error and achieve the target speed. The output of the PI controller was connected to a transfer function such that if the error were positive the vehicle would accelerate, and if the error were negative the vehicle would brake. Based on calculated acceleration and brake pedal percentages, torque would be demanded from the engine and motors and the brake force required to retard the vehicle would be recalculated.

The drive-mode selector was based on the hybrid vehicle described by Mechtenberg (2009). A stateflow controller was developed to select the driving modes of the vehicle, based on the vehicle speed (Golbuff, 2006). At low-speed/high-torque maneuvers (between 0 to 25 kph), the traction motor was used to power the vehicle. A motor-generator system provided power between the speeds of 25 kph and 50 kph. At vehicle speeds higher than 50 kph but less than 100 kph, three cylinders of a V6 engine were powered by

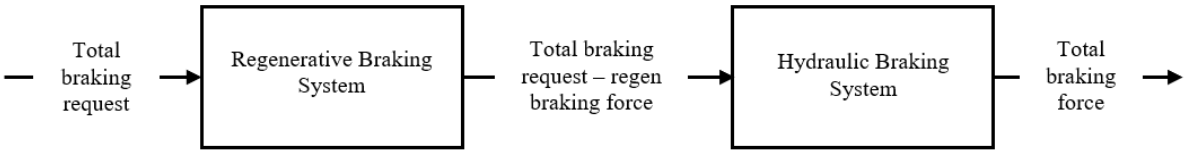

Figure 4. Schematic of a series HEV.

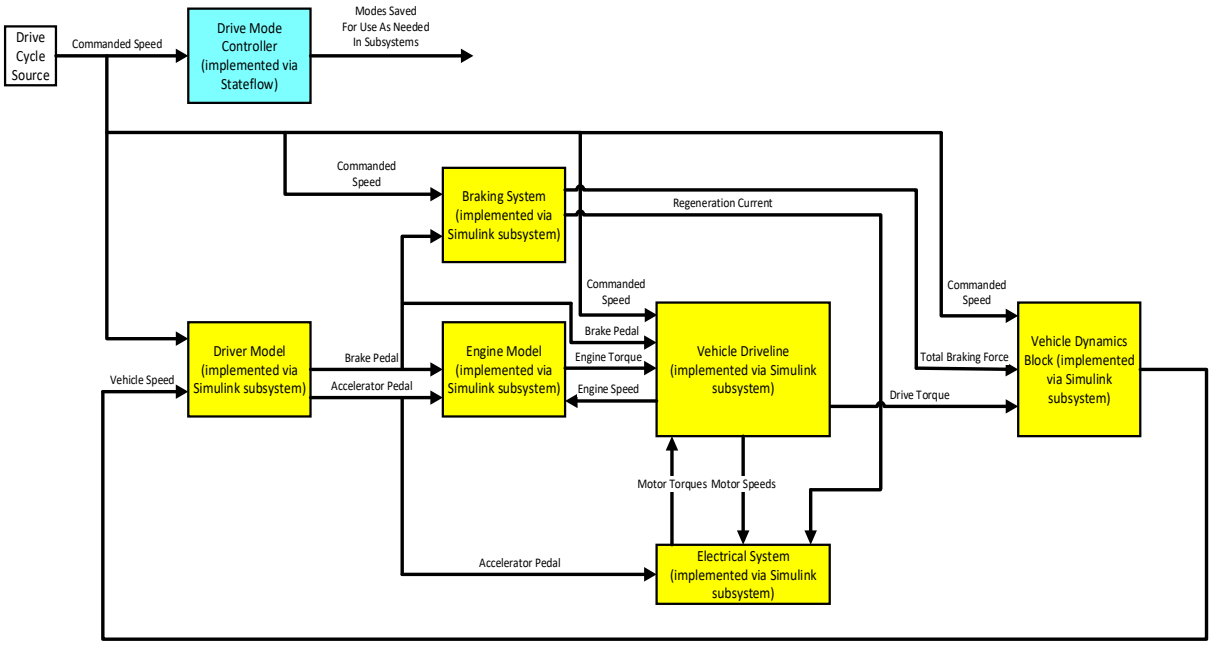

Figure 5. Overview of the multi-mode plug in hybrid electric vehicle model.

gasoline. The other three cylinders were powered by a sustainable fuel source when the vehicle's speed was between100 kph and 130 kph. If the vehicle speed was above 130 kph, the engine used gasoline and a sustainable fuel source to power the vehicle.

The simulation model of the engine and electrical systems was developed using a quasi-static approach, based on the simulation targets and powertrain characteristic of the model (Millo, Rolando & Andreata, 2011). The output to be delivered by each of the power systems was torque (i.e., engine torque when the engine was running and a motor torque when the motors were selected), which was determined by interpolation of steady-state performance maps from the inputs of the accelerator, brake, and engine/motor speed data.

In a parallel hybrid, the torque from the engine must combine with the torque from the electric motors to meet the requirements for propulsion (Che, Tsou, Rose & Jennings, 2009). The vehicle switches power sources between engine and motors based on the control system demand of the drive-mode selector. A planetary gear train was utilized to combine all the sources of power, while the engine was connected to the ring gear and the motor-generator to the sun gear. The traction motor was connected to the differential via a simple gearbox arrangement. To have seamless torque delivery in the transmission model, a clutch was modeled to engage and disengage the IC engine, motor-generator, and traction motor independently from the respective gearboxes.

Braking System

The braking subsystem functioned as the brake control unit (BCU) of the model. The brake percentage input from the driver triggered the BCU. Total braking force requested by the driver to retard the vehicle was estimated from the percentage of the brake pedal pressed. From Newton's second law, the braking rate was calculated based on Equation 10:

$$\frac{RBF}{Weight} = \frac{a}{g} \tag{10}$$

where, *RBF* is the requested brake force, a is the deceleration of the vehicle, and g is the acceleration due to gravity.

Figure 6 shows the calculated brake rate that was provided to the brake mode selector. The brake mode selector was designed based on the principles set forth by Gao et al. (1999). A front-wheel-drive passenger car under normal driving procedures would decelerate within the range of 0.1-0.3g. This is the region in which maximum regenerative braking should occur. At lower g-forces, the vehicle is able to come to a slow halt or just reduce its speed, whereas at high g-force values (above 0.6) the vehicle needs to stop in the shortest distance possible or retard in a short time span. These requirements were incorporated into the algorithm. Figure 7 shows that, at a small braking rate ($a/g \leq 0.1$), only regenerative braking on the front axle is activated, as depicted by AB. To ensure the stability of the vehicle, in the case where the braking rate is in the range of $0.1 < a/g < 0.3$, the

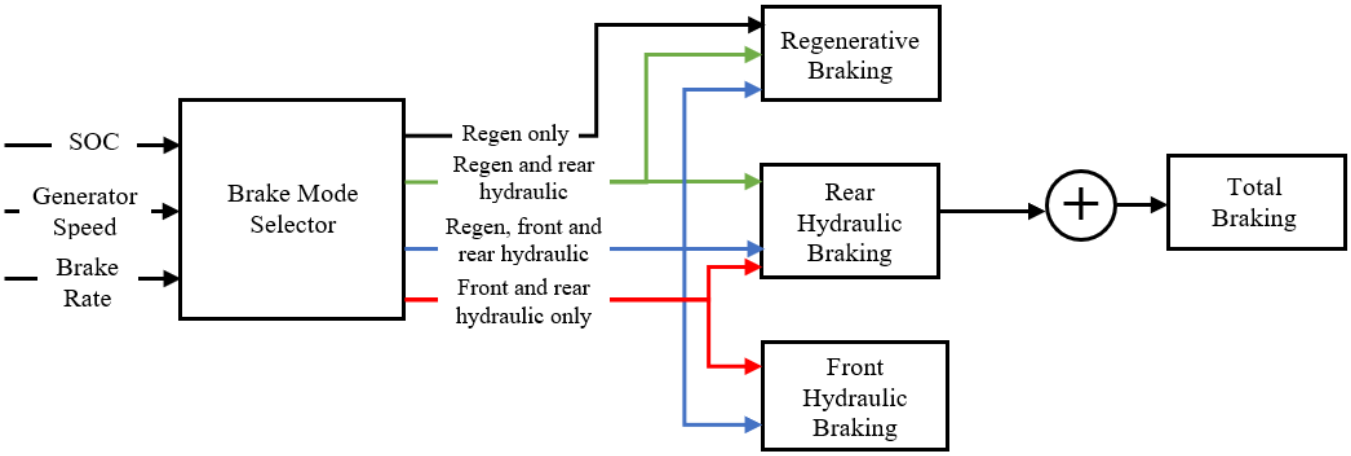

Figure 6. Schematic of the brake controller.

front axle would use a regenerative braking force and the rear axle hydraulic braking force would be activated, which would produce the brake force distribution curve between points B and C. When the requested braking rate is in the higher range, $0.3 < a/g < 0.6$, there is a higher priority on stopping the vehicle quickly. Due to the increase in brake force demand, the front hydraulic braking force works simultaneously with regenerative braking on the front axle, and rear hydraulic braking is active, producing the curve from point C to D. In cases where the braking rate is greater than 0.6g, it is considered an emergency braking condition, where stopping the vehicle in the shortest distance is the priority. To stop the vehicle in the shortest possible distance, brake force distribution should be equal to the optimum/ideal brake distribution. In this case, only hydraulic braking on the front and rear axles is given priority. Thus, points D and E lie on the optimum/ideal force distribution curve.

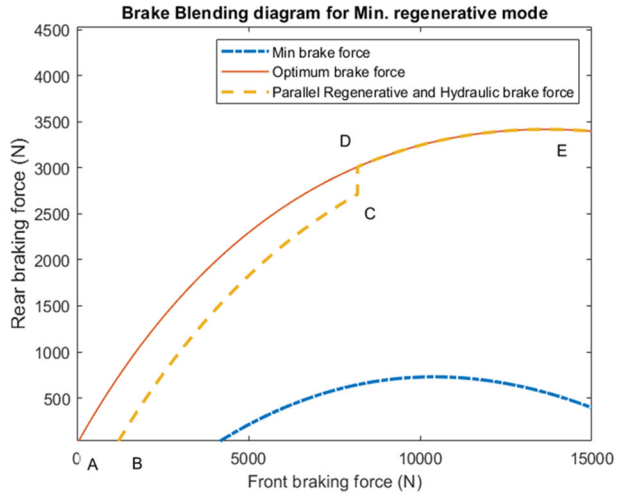

Figure 7. Brake force distribution curve for minimum regeneration mode.

Figure 6 shows that, apart from brake rate values, regenerative braking is also dependent on the state of charge (SOC) of the battery and on generator speed. If the SOC of the battery is above 80%, the vehicle would not be charged further through regenerative braking. If the generator speed is higher than the rated base speed, the amount of torque the generator can produce is limited. The generator cannot generate enough current to deliver back into the shallow-charge battery, due to the losses the current must overcome. To deliver the total braking force requested by the driver model, the braking option was selected by the brake mode selector. The regenerative braking force to be delivered was dependent on the torque that could be produced by the generator at the given generator speed, as given by Equation 11:

$$F_{gen} = \frac{T_{gen}\eta_{gen}GearRatio}{WheelRadius} \tag{11}$$

where, T_{gen} is the generator torque for the specified generator speed, η_{gen} is the efficiency of the generator, and F_{gen} is the braking force.

Since the generator can deliver the same torque at multiple motor speeds, and to prevent cases of over braking, F_{gen} was compared with the force required on the front axle for the requested brake rate. If F_{gen} was greater than or equal to the requested front axle braking force, then the output had to be the value of the requested front axle braking force, otherwise, the output had to be F_{gen}. The front and rear hydraulic braking forces were then calculated from Equations 12 and 13.

$$F_{wgt,F} = F_{weight}\left(1 - \Psi + \frac{a}{g}X\right) \tag{12}$$

$$F_{wgt,R} = F_{weight}\left(\Psi - \frac{a}{g}X\right) \tag{13}$$

Based on the mode of braking selected, the braking forces generated per axle were calculated. And, finally, the regenerative braking torque provided by the generator and the friction braking force generated by the hydraulic brakes would meet the total brake request of the vehicle.

Vehicle Dynamics

A one-dimensional vehicle dynamics block was built in MATLB/Simulink to predict the tractive forces required by the vehicle. The model determined the dynamic weight shifts during acceleration and braking. Figure 8 shows the entire brake control algorithm, including the various decisions noted above and the integration of vehicle dynamics. Brake blending must have a seamless delivery of force. If the brake force delivered to the driver is either higher or lower than demand, the consequences could be severe. To prevent cases of over-braking and under-braking, a brake system unit test was performed to evaluate the performance of the brake blending algorithm by pressing the brakes from 0-100%. Figure 9 shows the forces generated at various pedal percentages.

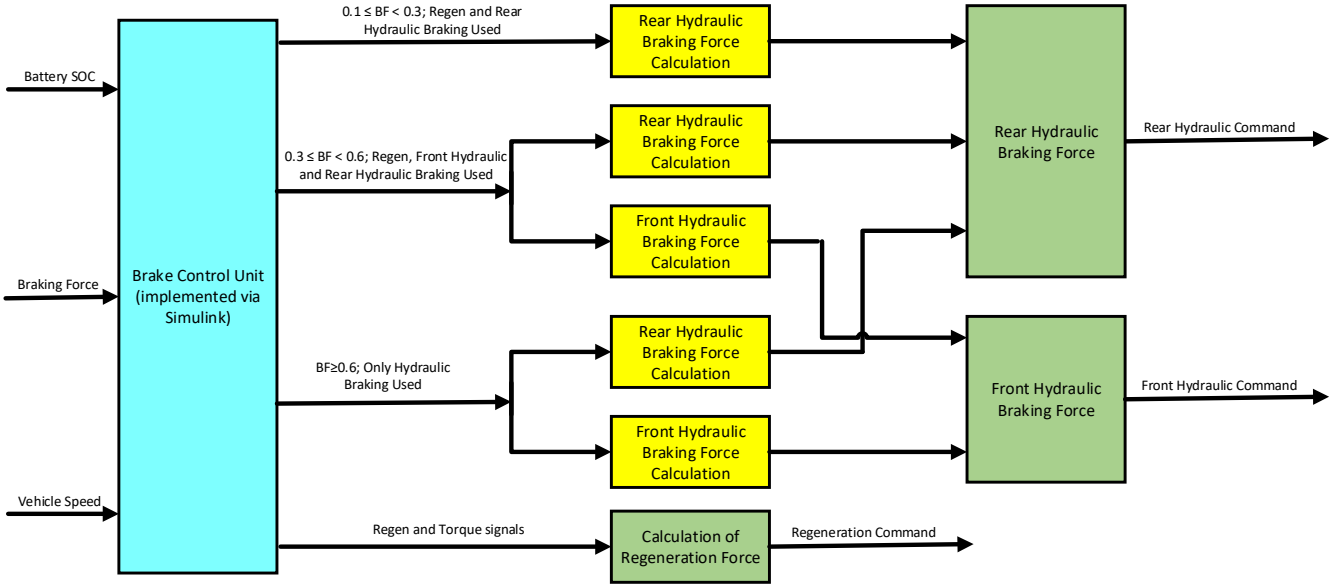

Figure 8. Top-level view of the brake control algorithm simulation and results.

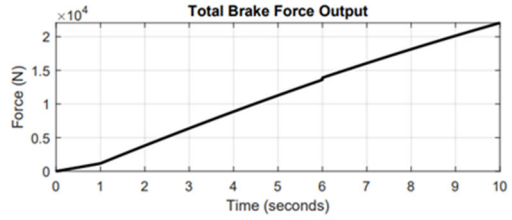

(a) Total brake force.

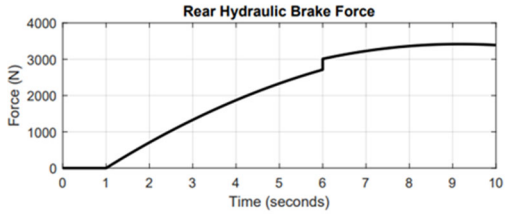

(b) Rear hydraulic brake force.

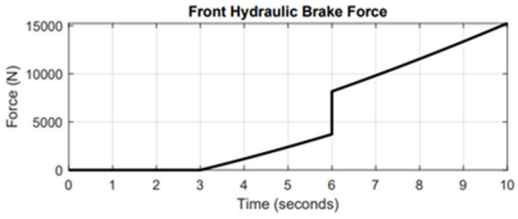

(c) Front hydraulic brake force.

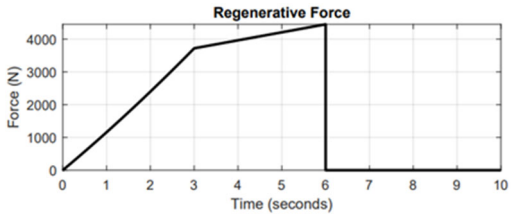

(d) Regenerative brake force.

Figure 9. Force distribution during a brake blending test.

The prime function of a braking system is to stop the vehicle within a given distance. When the driver demands brake force to retard or stop the vehicle, it means to deliver the required force under ideal conditions and stop the vehicle within the least possible distance. When parallel regenerative braking is in the system, the vehicle's braking system has an additional function for conserving energy; however, it is essential that this energy be recaptured, though it should be noted that conservation does not compromise vehicle safety.

The ECE R13 regulation calls for a braking performance test where the vehicle is tested on a track for the emergency condition—the vehicle's stopping distance is measured confirmed to be within the specified limits. The performance braking test conditions state that the distance covered by the vehicle from the moment when the driver begins to actuate the control of braking systems shall be evaluated until the vehicle stops. The brake system's performance is measured by determining how far the vehicle travelled before coming to a stop. As per the regulation followed for testing, the stopping distance is based on accelerating the vehicle to 160 kph (100 mph) and then applying the brake at 100%. This test was conducted on a track with a coefficient of friction equal to 0.9. The stopping distance for the vehicle is given by Equation 14:

$$\text{Stopping Distance}(m) \le 0.1V + 0.0067V^2 \qquad (14)$$

where, V is the initial vehicle speed (i.e., 160 kph) with the requirement that the stopping distance must be less than or equal to 171.52m when the brakes are applied at 100%.

Additionally, the test was conducted across various modes of regenerative braking, namely: pure hydraulic, minimum regenerative braking, medium regenerative braking, and high/maximum regenerative braking. Figures 10 and 11 show a brake blending curve for each of the braking modes, with Figure 10 showing the medium regenerative braking mode and Figure 11 showing the maximum regenerative braking mode. Figure 12 shows a test pattern similar to the brake performance test that was simulated where the vehicle was accelerated to 100 mph (160 kph), maintained at that speed for 25s, then the brake pedal was depressed. Instead of performing the test for only 100% braking, the vehicle's stopping distance was measured at all load cycles. It was assumed that the driver would depress the brake and hold it at a constant brake percentage. The results of the simulated brake performance test were based on a few assumptions:

- The driver's reaction time for braking remained same in all cases.
- There was no condition for wheel lock up.
- The environmental factors remained the same.

All the aforementioned regenerative modes used above-minimum brake forces. To determine the optimum tradeoff between braking distance and energy conservation, the brake performance test was run for various load cycles. Results were utilized to determine which mode of regenerative braking would aid in recuperating energy and as well as stopping the vehicle in a significantly shorter distance. Figure 12 shows the results of one such test cycle in which a single load was run with different modes and pedal rates and with the brake applied at 70 seconds.

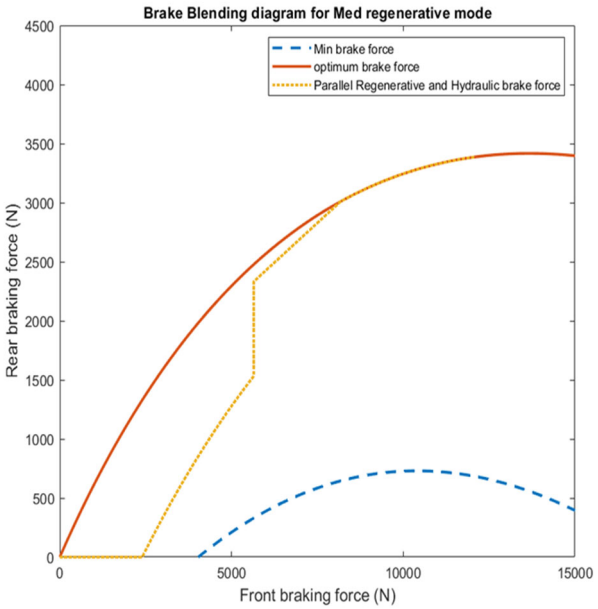

Figure 10. Brake blending curve for medium regenerative braking mode.

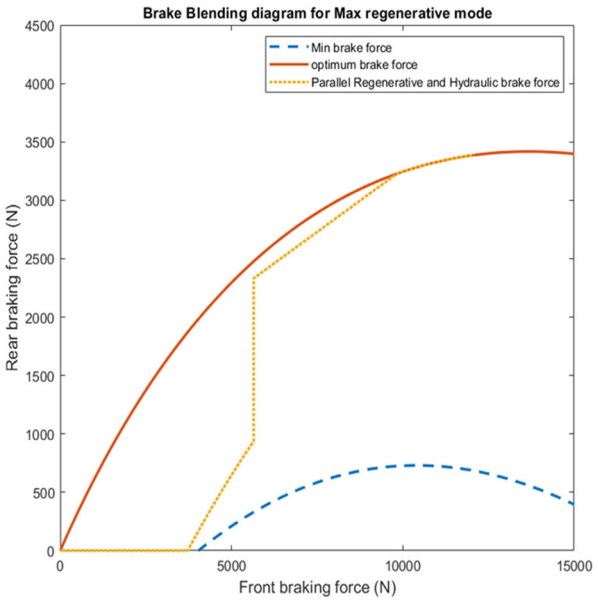

Figure 11. Brake blending curve for maximum regenerative braking.

Results of Performance Brake Tests

As per the BCU control algorithm, when the brakes were pressed to 100%, an emergency braking condition was triggered and provided stopping in the shortest possible distance using only hydraulic braking. The vehicle stopped in 67.02m, below the regulation-mentioned standard of 171.52m.

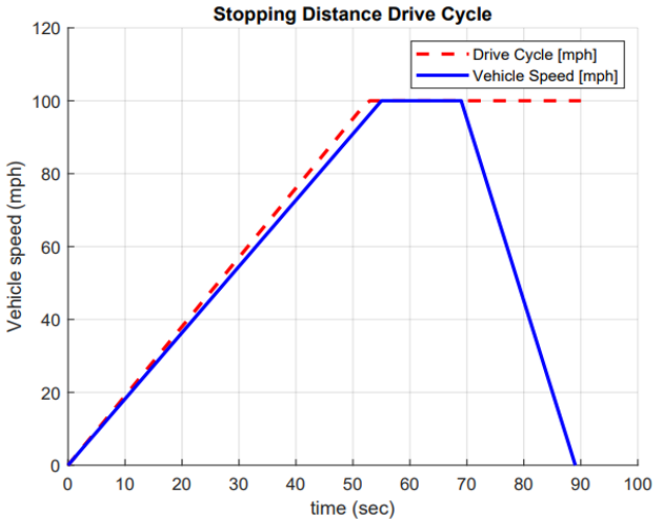

Figure 12. Brake performance test cycle for a single load.

Figure 13 shows that, at various pedal rates and regenerative modes, the energy conserved by regenerative braking was calculated for a variety of different levels of regeneration. Logically, one would prefer to have minimum stopping distance together with the maximum energy conservation, which would indicate that points in the lower right part of the graph would be desirable. In the lower part of the graph, it can be seen that there was a tradeoff between energy conservation and stopping distance, with greater stopping distance being the price of increased energy conservation. The medium and maximum regeneration values were very similar to each other in this part of the graph, with only minimal differences between them as they tradeoff which curve was optimal in various ranges. It was also noted that, at a certain point, no further energy could be recovered; some pedal rates were not desirable, as they resulted in both less energy conservation and a longer stopping distance. At those lower pedal rates, the minimum regeneration gave better results than the medium or maximum regeneration, although overall even the "better" results were not optimal compared to those seen with higher pedal rates.

The HEV model was then tested for four different urban drive cycles: the Urban Dynamometer Driving Schedule (UDDS), New York City Cycle (NYCC), Japan 10-15, and Braunschweig city driving cycle. City cycles were chosen for testing the regenerative braking of the system, as they were expected to require more brake usage than highway driving. Figures 14-17 show the results of each test cycle. The first plot in each figure, shown at the top, demonstrates that the speed of the vehicle in the model did match that of the commanded drive cycle. In the lower plot in the figures, the total braking force is shown. The majority of the braking in these urban driving scenarios can be accomplished purely from regenerative braking, resulting in little wasted energy.

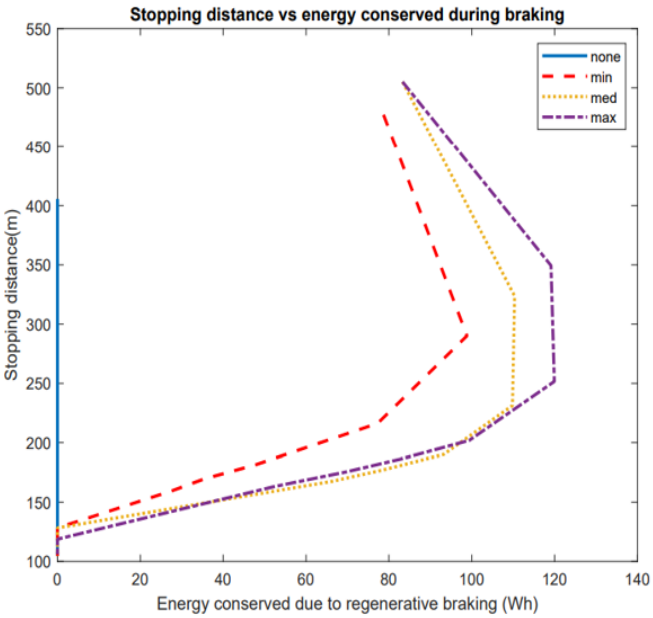

Figure 13. Vehicle stopping distance versus energy conserved during braking in different modes.

Table 2 shows a summary of the results of these cycles, simulated with and without regenerative braking in order to observe the change in energy consumption. The amount of energy recovered is expressed in percentage.

Conclusions

Among all the different modes of regenerative braking tested, the medium regenerative braking system had the potential to provide sufficient braking force to safely drive the vehicle as well as increase the energy conserved across all driving cycles. The MIL simulation results for multiple city-driving cycles showcased the advantages of a regenerative braking control algorithm. The energy usage for vehicles with the minimum regenerative braking strategy in the NYCC was observed to be 15% less than the proposed regenerative braking algorithm. Similarly, when tested for other city driving patterns, such as UDSS, Japan 10-15, and Braunschweig city driving cycle, the energy usage of the minimum regenerative braking was observed to be 12%, 3%, and 7% lower, when compared to the medium regenerative braking algorithm. The results shown here can be used to design better braking algorithms in order to receive the maximum benefit from regenerative braking systems based on a particular vehicle and its use cases.

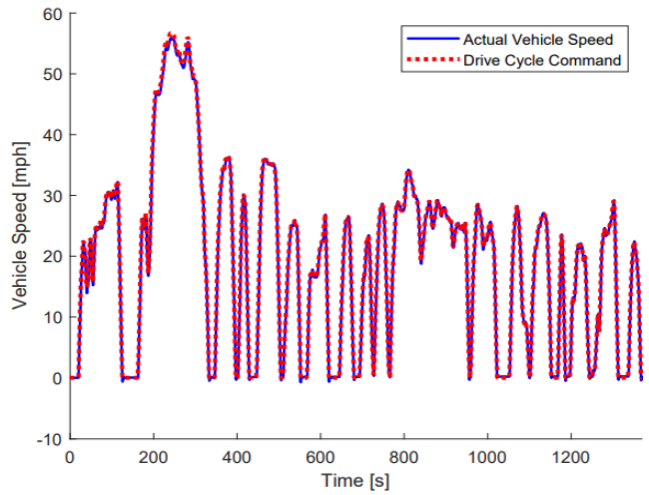

(a) Comparison of drive cycle command and actual vehicle speed.

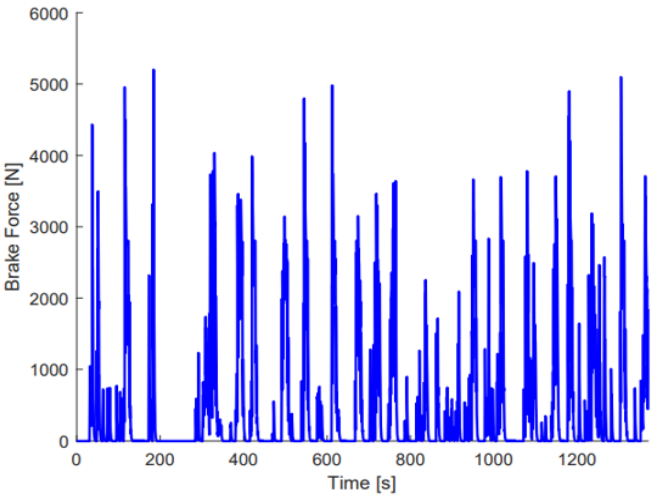

(b) Total braking force.

Figure 14. Vehicle velocity and total braking force delivered for the UDDS drive cycle.

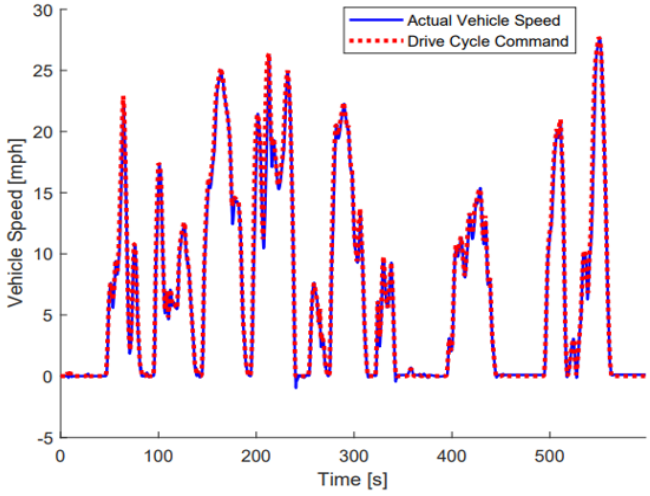

(a) Comparison of drive cycle command and actual vehicle speed.

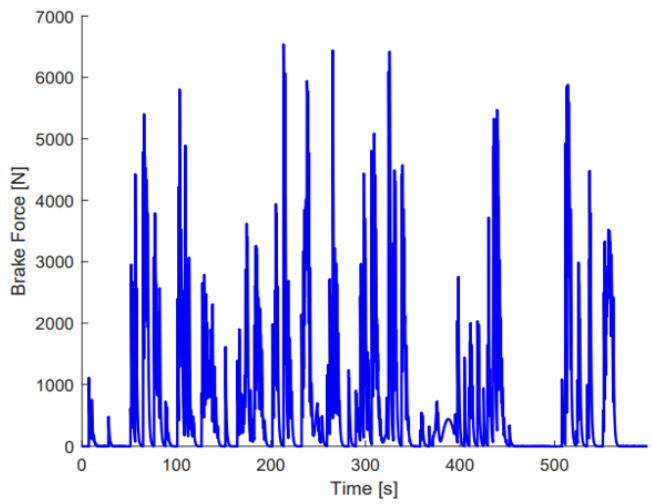

(b) Total braking force.

Figure 15. Vehicle velocity and total braking force delivered for the NYCC drive cycle.

Table 2. Comparison of energy consumption for drive cycles with and without regenerative braking.

		Drive Cycle			
	Unit	UDSS	NYCC	Japan 10-15	Braunschweig city driving cycle
Time of drive cycle	sec	1369	598	660	1740
Distance	km	11.99	1.89	4.17	10.88
Energy consumed with only hydraulic braking system	kWh	3.879	0.823	0.856	3.137
Energy conserved by minimum regenerative braking system	kWh	0.761	0.190	0.276	0.778
Energy conserved with medium regenerative braking system	kWh	0.851	0.219	0.283	0.833
Energy conserved with maximum regenerative braking system	kWh	0.948	0.228	0.284	0.880
% change in energy conserved between minimum and medium regenerative braking	%	12	15	3	7

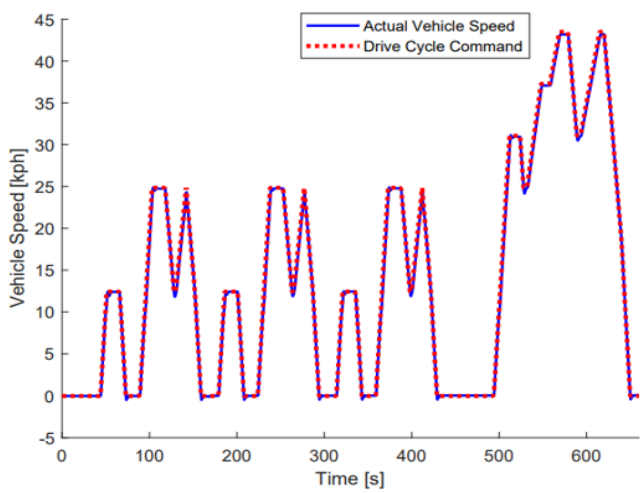

(a) Comparison of drive cycle command and actual vehicle speed.

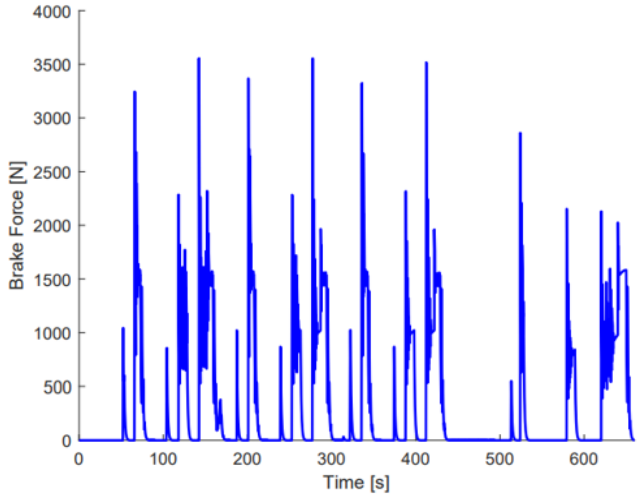

(b) Total braking force.

Figure 16. Vehicle velocity and total braking force delivered for the Japan 10-15 drive cycle.

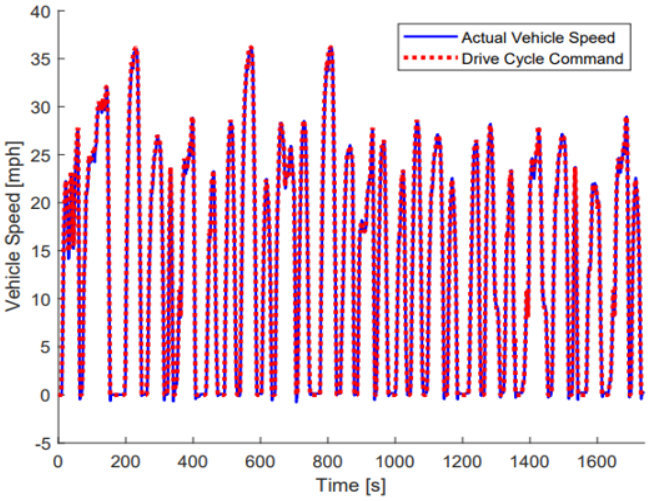

(a) Comparison of drive cycle command and actual vehicle speed.

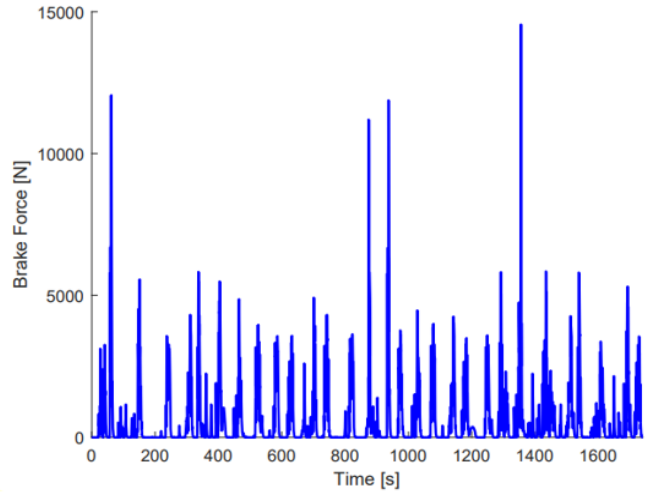

(b) Total braking force.

Figure 17. Vehicle velocity and total braking force delivered for the Braunschweig city drive cycle.

References

Boerboom, M. (2012). Electric vehicle blended braking: Maximizing energy recovery while maintaining vehicle stability and maneuverability. [Master's thesis, Chalmers University of Technology]. https://odr.chalmers.se/handle/20.500.12380/155034

Breuer, B. J., & Bill, K. (2008). *Brake technology handbook*. SAE International.

Che, J., Tsou, P., Rose, L., & Jennings, M. (2009). Modeling and simulation of the dual drive hybrid electric propulsion system. (No. 2009-01-0147). SAE Technical Paper.

Ehsani, M., Gao, Y., Longo, S., & Ebrahimi, K. (2018). *Modern electric, hybrid electric, and fuel cell vehicles.* CRC Press.

Gao, Y., Chen, L. & Ehsani, M. (1999). Investigation of the effectiveness of regenerative braking for EV and HEV. *SAE transactions*, 3184-3190.

Golbuff, S. (2006). *Optimization of a plug-in hybrid electric vehicle* (Master's thesis, Georgia Institute of Technology). http://www.ehcar.net/library/these/these031.pdf

Regulation No. 13-H-01: Passenger Car Braking. InterRegs. https://www.interregs.com/catalogue/details/ece-13h01/regulation-no-13-h-01/passenger-car-braking/

Mechtenberg, A. (2009). *Understanding the importance of an energy crisis* (Doctoral dissertation, University of Michigan). https://deepblue.lib.umich.edu/handle/2027.42/63801

Mechtenberg, A. R., & Peters, D. L. (2012). Control of a 36 mode hybrid vehicle with driver option selection: Incorporating urban, suburban, and highway driving. In *Dynamic Systems and Control Conference, 45295*, 137-144. American Society of Mechanical Engineers.

Millo, F., Rolando, L., & Andreata, M. (2011). Numerical simulation for vehicle powertrain development. In *Numerical Analysis-Theory and Application*. IntechOpen. DOI: 10.5772/24111

Raut, A., Phalke, S,. & Peters, D. L. (2019). Modeling and control of new multi-mode plug-in hybrid electric vehicle. Paper presented at the International Design Engineering Technical Conferences and Computers and Information in Engineering Conference (Vol. 59216, p. V003T01A042). American Society of Mechanical Engineers.

Wang, Y., Wu, Z., & Feng, K. (2019). Comparative analysis of series and parallel regenerative braking control strategies. *Open Journal of Circuits and Systems*, *8*(3), 50-55. https://doi.org/10.12677/ojcs.2019.83007

Biographies

ANEESH SURI is a Powertrain Engineer II at Mercedes-Benz Research & Development North America, Inc. He earned his Bachelor of Technology in Mechanical Engineering from GITAM University in 2014 and his MS from Kettering University in 2020. Mr. Suri may be reached at aneeshsuri1992@gmail.com

DIANE PETERS is an Associate Professor of Mechanical Engineering at Kettering University. She earned her BS from the University of Notre Dame in 1993, her MS from the University of Illinois–Chicago in 2000, and her PhD from the University of Michigan in 2010. Dr. Peters' research interests include combined design and control and autonomous vehicles. Dr. Peters may be reached at dpeters@kettering.edu

Review of Surrogate Safety Measures for Roadway Safety Analysis

Nathaniel Edelmann, Boise State University; Mandar Khanal, Boise State University

Abstract

Motor vehicle accidents—or MVAs, as referred to by the medical community—are a source of tremendous costs in the form of financial damages, human injuries, and deaths. Because of this, traffic safety is of utmost importance to engineers, as they design transportation infrastructure. Traffic safety analyses provide detailed information for civil engineers to make decisions relating to projects intended to bolster the safety of roadways and intersections. These analyses use data that is collected for a transportation system network. The traditional method of safety analysis uses collision data, but a newer set of safety analysis methods instead considers data on traffic conflicts as a replacement for collisions. These methods are known as surrogate safety measures (SSMs) that analyze kinematic data to assess safety. Several SSMs have been developed and validated in an effort to more fully capture the risk exposure of vehicles. SSMs offer a range of benefits over traditional analyses with collision data.

First, the data used by SSMs may be collected more rapidly than collision data. Collisions happen quite infrequently from a data collection standpoint, but vehicular kinematic data may be collected in large quantities within a matter of weeks. Second, surrogate safety measures are a proactive analysis, as they allow for safety analyses without the need for actual collisions to occur. Improvements may be made based upon the results of an SSM analysis to prevent crashes. Third, kinematic data supply many more data points, as opposed to collisions, which make statistical analyses for traffic conflicts significantly more robust. Analyses with SSMs have evolved over the decades from being measured with manual observations in the field using time-lapse imagery, to the use of microsimulation software with the most recent advancement being the incorporation of connected vehicle data. In this paper, the authors provide a summary of the development of SSMs that have been used to establish the state of practice for surrogate safety analysis.

Introduction

Surrogate safety measures (SSMs) are a means of measuring the safety of traffic infrastructure using data other than crash data. SSMs are beneficial because they eliminate the need to wait, oftentimes for long periods of time, for crashes to occur and generate data. In a similar vein, the use of SSMs allows for hazardous areas to be identified prior to a large number of crashes occurring. This may mean that improvements can be made earlier to prevent those crashes. Yet another benefit of using SSMs is the dramatic increase in data points that comes from being able to analyze traffic conflicts instead of collisions. Conflicts are extremely common, whereas collisions are quite rare by comparison for an individual location. And, more data points allow statistical analysis to be more effective.

One class of current research pertaining to SSMs involves the investigation of harsh braking events recorded by connected vehicles as an SSM. The validity of harsh braking as an SSM will need to be investigated in order to determine if its use is indeed viable. Such validation may be done through the comparison of results of a safety analysis conducted with the harsh braking SSM to historical crash counts, or to the results of a safety analysis conducted using existing SSMs. The articles and reports included within this paper offer insight into how SSMs have evolved over time and how new SSMs may be validated. Similarly, they illuminate the various mechanisms used to compute the safety of road infrastructure as alternatives to crash data.

The following sections provide summaries of pertinent content within a selection of articles and reports published on SSMs in transportation engineering. The literature reviewed includes a paper that uses SSMs in conjunction with connected vehicle data, papers that define SSMs founded in both kinematics and statistics, papers on the use of SSMs with traffic microsimulation software, and even two papers that establish new SSMs and validate them through the use of microsimulation (Wang & Stamatiadis, 2013; Astarita, Caliendo, Giofré & Russo, 2020). This information is presented together in one paper to serve as a resource for researchers and practitioners alike to understand the current state of this research and the means by which these methods have been established.

Paper #1:
Analysis of Traffic Conflicts and Collisions

In the first paper reviewed (Allen, Shin & Cooper, 1978), the authors, from McMaster University in Canada, set out to improve upon the previously established traffic conflicts technique (TCT). They outline a number of flaws with TCT and propose several SSMs that would ameliorate the shortcomings of TCT as it existed previously. Their newly established SSMs include proportion of stopping distance, gap time, encroachment time, deceleration rate, post-encroachment time, and initially attempted post-encroachment time. The paper begins with the discussion of the existing TCT and the areas in which it lacks effectiveness. Prior to this paper, TCT used brake applications as the primary indicator of a traffic conflict. While

brake applications are easily identified and counted without subjectivity in the data analysis process, they have several drawbacks. Drivers have variable braking habits with overly cautious drivers applying brakes when it is not necessary and less cautious drivers failing to apply brakes during hazardous encounters. Brake applications are also a binary measurement with no indication of the severity of the evasive maneuver. Finally, deceleration is not always an effective evasive maneuver. Sometimes acceleration is the safest option in order for a vehicle to clear a potential collision location. This can lead to an inaccurate conclusion in TCT. A traffic conflict definition can be misleading if it relies on the presence of an evasive maneuver, such as brake application. This is because collisions can occur without any evasive maneuver taking place. This means that a traffic conflict definition requiring evasive action can lead to collisions that are not preceded by a conflict.

This is problematic because collisions are supposed to be a subset of conflicts. Allen et al. (1978) suggest that measurement of various parameters within the time-space diagram would be useful for safety analysis, and they present several measures that they developed based on the time-space diagram. The diagram displays a through vehicle, beginning at time T_0, that slows upon the appearance of a left-turning vehicle ahead at time T_1. The left-turning vehicle encroaches on the space ahead of the through vehicle until time T_2, at which time the through vehicle accelerates back to its top speed. The through vehicle reaches the location of the encroachment at time T_4.

In addition to these times, as indicated in their diagram, the through vehicle's original motion is projected to illustrate when the through vehicle would have reached the location of the encroachment had that encroachment never taken place. This time is labeled T_3. The motion of the vehicle at time T_2, when the encroachment ends, is also projected to illustrate when the through vehicle would have reached the location of the encroachment had it not accelerated back to its top speed. This time is labeled T_5. The location of the through vehicle at the beginning of the encroachment is labeled P_1, and its location at the end of the encroachment is labeled P_2. The location of the encroachment is labeled P_3 (Allen et al., 1978).

The paper outlines SSMs developed by Allen et al. (1978) as alternatives to TCT based primarily on brake applications. The first measure is proportion of stopping distance (PSD), which is the ratio of the remaining distance between a vehicle and a potential collision point to the minimum acceptable stopping distance. The PSD must be at or above a value of 1.0 for a situation to be safe, and can be found using Equations 1 and 2 (Allen et al., 1978):

$$PSD = \frac{RD}{MSD} \tag{1}$$

$$MSD = \frac{V^2}{2D} \tag{2}$$

where, *RD* is the remaining distance between a vehicle and a potential collision point, *MSD* is the minimum acceptable stopping distance, *V* is the following vehicle's velocity, and *D* is the maximum acceptable deceleration rate.

The next measures described were gap time (GT), encroachment time (ET), and deceleration rate (DR). GT is the difference between T_3 and T_2, as previously described. Time T_3 is the time at which a through vehicle would have arrived at the potential collision point if the through vehicle had not altered its motion. Time T_2 is the time at which the left-turning vehicle is no longer encroaching on the through vehicle's path of travel. GT can, therefore, be positive or negative. A smaller absolute value of GT represents a greater probability of a collision occurring. ET is a measure of the total amount of time that the left-turning vehicle occupies the path of travel of the through vehicle, the difference between T_2 and T_1. DR is another SSM that occurs through the development of a conflict and is capable of indicating situational severity. Allen et al. (1978) point out that variability between drivers can account for higher or lower DRs to some extent. However, rapid deceleration is a strong indicator of a hazardous situation.

The last two developed measures were post-encroachment time (PET) and initially attempted post-encroachment time (IAPE). PET is the amount of time that elapses between when an encroaching vehicle leaves the path of travel of another vehicle and when the other vehicle reaches the point where a collision would have occurred. PET may be quantified as the difference between T_4 and T_2. PET represents how narrowly drivers avoided colliding. The measure represents the cumulative effects of the initial situation and the actions taken by the drivers to avoid colliding. PET suffers from drivers often accelerating as soon as a conflict ends. For this reason, Allen et al. (1978) developed IAPE, which eliminates the effects of early acceleration. IAPE may be calculated using Equations 3 and 4:

$$IAPE = T_5 - T_2 \tag{3}$$

$$T_5 = T_1 + \left(P_1P_3 / V_2\right) \tag{4}$$

where, T_1 is the beginning time of encroachment, P_1P_3 is the distance between the potential collision point and the initial location of the through vehicle, and V_2 is the average through vehicle velocity.

Allen et al. (1978) further suggested that the most controversial part of their paper was the rejection of the TCT brake application method. They conceded the point that their evaluation of their new SSMs was not highly effective in confirming an advantage in these measures. This is because the correlation coefficients obtained for the SSMs were low, in spite of an active collision history at the study intersection. Little hope exists to have higher correlation coefficients at any intersection. Low correlation coefficients may be something to be expected, and arguments for a tran-

sition away from brake applications should rely on the conceptual weaknesses of brake applications. The fact that not all collisions are preceded by braking should alone bar brake application from being an acceptable measure (Allen et al., 1978).

Paper #2:
Extended Time-to-Collision Measures for Road Traffic Safety Assessment

In this next article, Minderhoud and Bovy (2001) outline the development of two new modifications to a surrogate safety measure known as time-to-collision (TTC). Minderhoud and Bovy called these modifications "Extended Time-to-Collision" together, and individually these modifications were called "Time Exposed Time-to-Collision" and "Time Integrated Time-to-Collision." Their paper addressed the use of these measures with vehicles that were equipped with autonomous intelligent cruise control (AICC). These new measures were intended to provide a comparative measure that could be used in conjunction with microsimulation to understand the impacts to safety of the use of AICC.

Minderhoud and Bovy (2001) described the TTC SSM. TTC is the amount of time that would need to elapse in order for two vehicles to collide, if their trajectories remained unchanged. TTC can be calculated using Equation 5 (Minderhoud & Bovy, 2001):

$$TTC_i = \frac{X_{i-1}(t) - X_i(t) - l_{i-1}}{X_i'(t) - X_{i-1}'(t)} \forall X_i'(t) > X_{i-1}'(t) \qquad (5)$$

where, X is the vehicle's position, X' is the vehicle speed, and l is the vehicle length; also, the leading vehicle is denoted as i-1, and the following vehicle is denoted as i.

TTC may only be calculated for situations in which the speed differential between the vehicles is such that the leading vehicle is traveling more slowly than the following vehicle. The safety of a TTC value is tied to a critical TTC safety threshold. TTC values above this threshold are safe situations, and TTC values beneath this threshold are unsafe. Past research has produced threshold values ranging from 2.6 seconds to 4 seconds (Minderhoud & Bovy, 2001). Minderhoud and Bovy (2001) presented their modifications, beginning with time exposed time-to-collision (TET). TET is a summation of the time that the TTC is beneath the safety threshold value. A low TET value indicates a safe situation, because the overall exposure to a hazardous situation is small. It does not consider how severely the safety threshold is being violated. Calculation of TET requires position and speed data for all vehicles on a road section within the study time period. These data are typically collected at discrete moments, separated by a time-scan interval. TET may be calculated using Equation 6. For N number of drivers, the population TET* may be found using Equation 7 (Minderhoud & Bovy, 2001):

$$TET_i^* = \sum_{t=0}^{T} \delta_i(t) \cdot \tau_{sc} \text{ where } \delta_i(t) = \begin{cases} 0 \text{ else} \\ 1 \forall 0 \le TTC_i(t) \le TTC^* \end{cases} \qquad (6)$$

$$TET^* = \sum_{i=1}^{N} TET_i^* \qquad (7)$$

where, TTC^* is the safety threshold value of TTC, $TTC_i(t)$ is the value of TTC at a discrete time t for vehicle i, $\delta_i(t)$ is a switch variable that indicates if the threshold TTC is exceeded, and τ_{sc} is a time scan interval indicating the time step resolution.

Next, the paper presented the time integrated time-to-collision (TIT) SSM. The TIT measure addresses one drawback of the TET metric, its inability to consider the amount by which the safety threshold TTC is not met. In this way, TIT is capable of capturing the severity of the hazard better than TET. TIT can be calculated for continuous time using Equation 8. Analysis using continuous time is not practical; thus, Equation 8 represents a theoretical abstraction. For discrete time, TIT may be calculated using Equation 9 (Minderhoud & Bovy, 2001):

$$TIT^* = \sum_{i=1}^{N} \int_0^T \left[TTC^* - TTC_i(t) \right] dt \forall 0 \le TTC_i(t) \le TTC^* \qquad (8)$$

$$TIT^* = \sum_{i=1}^{N} \sum_{t=0}^{T} \left[TTC^* - TTC_i(t) \right] \cdot \tau_{sc} \forall 0 \le TTC_i(t) \le TTC^* \qquad (9)$$

Minderhoud and Bovy (2001) also present a graph that illustrates what TET and TIT measure. The graph displays TTC on the vertical axis and time on the horizontal axis. A horizontal line on the graph indicates the TTC safety threshold, TTC*. Curves on the graph show how the TTC changes for several situations. The sum of the linear durations of time that the curves are beneath the safety threshold is the TET. The sum of the areas between the curves and the line indicating the threshold is the TIT. These areas only exist where the curve is beneath the safety threshold. The graph illustrates the different units for TET and TIT. TET, being a linear duration of time on the graph, has units of seconds (sec). TIT, being an area on the graph, has units of seconds squared (sec^2).

Minderhoud and Bovy (2001) also used the comparative power of TET to demonstrate the impact of incorporating various levels of AICC. AICC is capable of adapting vehicle speed in order to maintain a proper distance from leading vehicles. To analyze the effectiveness of AICC, the researchers used an applied microscopic simulation with an individual driving behavioral model. They ran models for 50% partial AICC, 100% partial AICC, 50% complete AICC, and 100% complete AICC. Their analysis was also done for 1-second, 2-second, and 3-second safety threshold TTC values. They suggested that a shorter safety threshold TTC is possible for AICC because of its increased reaction ability over humans. Partial AICC requires driver intervention at speeds below 30 km/h or when the necessary deceleration is at or above 3 m/s^2. Complete AICC supports the

driver fully. Again, there was high exposure to high TTC values and low exposure to small TTC values. Choice of threshold TTC value had a large effect on the total exposure time. Choice of a realistic threshold depends upon the design of the AICC system; thus, there will be a waiting period until AICC systems are more established and empirical data are available. This may eventually be accomplished in future research.

Paper #3:
Surrogate Safety Measures from Traffic Simulation Models – Final Report

In this report by Gettman and Head (2003), the authors provide a summary of a project by the Federal Highway Administration that sought to evaluate the efficacy of the use of simulation software in conjunction with SSMs to determine the safety of intersections. It also identifies algorithms for determining SSMs from simulation models, known as the Surrogate Safety Assessment Methodology. This methodology allows for evaluation of various alternatives and is applicable to both signalized and unsignalized intersections. Gettman and Head (2003) presented descriptions of the following SSMs that are a part of the traffic conflicts technique: GT, ET, DR, PSD, PET, IAPE, and TTC. Field measurement is possible for these measures, but it introduces subjectivity that can compromise the quality of the safety analysis. Microsimulation can be used to simulate conflicts more precisely. There are other SSMs that have also been suggested. These measures include "delay, travel time, approach speed, percent stops, queue length, stop-bar encroachments, red-light violations, percent left turns, spot speed, speed distribution, and deceleration distribution" (Gettman & Head, 2003). Although these measures have not been quantitatively related to crash frequency, they may be used as indicators of higher or lower crash frequency. These informal measures exist for two-lane roads as well and include design features such as curvature and superelevation.

The report gives an overview of traffic simulation models. Microsimulations analyze traffic at the level of the individual vehicle over time steps. Vehicles in the simulation have varying characteristics, but they always drive safely and never crash. Gettman and Head (2003) favor microsimulations that are commonly used in industry and have analyses that are simple to implement. They also prefer the simulation to have a graphic network editor and analysis tools that may be used after processing. The analysis must model driver behaviors, such as car following, lane changing, and gap acceptance, and should have particularly realistic behavioral components in order to be useful. Most microsimulation programs do not readily allow extraction of data to output files, but this would be necessary for computing SSMs. The behavior and driver performance parameters need to be able to be manipulated, and the ability for a user to make or request modifications to the software itself at a relatively low cost is preferable. With these preferences established, Gettman and Head evaluated nine microsimulation programs: CORSIM, VISSIM, Simtraffic, Paramics, HUTSIM, Texas, WATSIM, Integration, and AIMSUN.

The evaluation of the various microsimulation software programs did not identify any clear best choice, but did reveal that using any microsimulation program for the computation of SSMs would require at least some modification of the program. Because of this, Gettman and Head recommended using a surrogate safety assessment module (SSAM) after the simulation is run. The workflow for conducting a safety analysis would involve running a simulation model, importing event files to the SSAM from the simulation, and then running the SSAM to generate reports and graphics detailing the computed SSMs. Gettman and Head went on to outline algorithms that allow SSMs to be computed for conflict events. Conflict events that may be modeled include crossing flows, merging crossing flows, adjacent flows (lane changing), and following flows (rear-end collisions). Some conflict events that were not modeled are sideswipe, head-on, and swerve-out-of-lane collisions as well as U-turn related and pedestrian collisions. Gettman and Head called for future research to improve the modeling of pedestrian collisions.

The report concluded with a discussion of validating SSMs as computed from microsimulations. One method of validation is determining if an SSM analysis with microsimulation may be used to decide between two different intersection design alternatives. The next way is to determine a correlation between SSMs and traditionally gathered crash data. The goal here was to determine if an SSM analysis with microsimulation could be used to replace traditional data-gathering procedures. The third way suggested by Gettman and Head to validate SSMs was to determine if it is possible to predict the benefits to safety caused by the implementation of safety-oriented intersection improvements. The report outlined methods for validating SSMs with microsimulation in these ways.

Paper #4:
Comparing Safety Performance Measures Obtained from Video Capture Data

In this paper by Guido, Saccomanno, Vitale, Astarita, and Festa (2010), the authors detail a study in which SSMs were calculated for a roundabout in an urban area of Cosenza, Italy. The SSMs used in this study included TTC, TIT, deceleration rate to avoid collision (DRAC), PSD, and crash potential index (CPI). The different outcomes of the safety analysis, according to the particular safety measure used, traffic conditions, and roundabout geometry variations, were discussed with the purpose of demonstrating the usefulness of SSMs and highlighting the impact of using different measures on the outcome of safety analysis. Next, Guido et al. discussed the SSMs that they used in the study. The first SSM described was DRAC. DRAC is based on the idea that a leading vehicle will execute some initial action,

such as braking, changing lanes, or accepting a gap. The following vehicle, in turn, decelerates in order to avoid a rear-end collision. Guido et al. used a DRAC safety threshold of 3.35 m/s^2. DRAC is an effective safety measure, because it considers the effects of differential speeds and evasive action in the form of braking. It can be calculated for rear-end collisions using Equation 10:

$$DRAC_{FV,t+1}^{REAR} = \frac{\left(V_{FV,t} - V_{LV,t}\right)^2}{\left(X_{LV,t} - X_{FV,t}\right) - V_{LV,t}} \quad (10)$$

where, t is the time interval, X is the position of the vehicle, L is the vehicle length, and V is the velocity; also, the subscript FV refers to the following vehicle, and the subscript LV refers to the leading vehicle.

Guido et al. next discussed TTC and PSD, as defined previously. The safety threshold for TTC was set at 1.5 seconds in that study. The paper went on to define and discuss TIT, which was presented here in the discussion of Paper #2. The final SSM discussed in the paper was CPI. CPI was developed in response to the identification of concerns with the original DRAC measure. DRAC has the drawback of not considering the variability of vehicle braking capacity based on mechanical variations in vehicles or environmental factors. To address these variations, the CPI was developed, which takes braking capacity variations into consideration. The DRAC and the maximum available deceleration rate, MADR, are calculated at every time step considered. CPI can be calculated using Equation 11 (Guido et al., 2010):

$$CPI_i = \frac{\sum_{t=ti_i}^{tf_i} P\left(DRAC_{i,t} > MADR_i\right) \cdot \Delta t \cdot b}{T_i} \quad (11)$$

where, Δt is the observation time interval, b is a state variable that equals 1 if the gap between the leading and following vehicles is closing and 0 otherwise, T_i is the total observed time for vehicle i, ti_i is the initial time interval observed, and tf_i is the final time interval observed.

The authors went on to outline the methods employed to measure the interactions of vehicles within the study roundabout. A camera was set up on the roof of a building close by and was used to record traffic operations on a weekday during off-peak hours. Off-peak hours were selected because the vehicular speeds are not reduced by congestion. Radar measurements revealed the average speed of vehicles to be 25 kph during the off-peak conditions. The Adobe Premier software program was used to process the video to obtain trajectories. In addition to the video footage, 176 virtual detectors were spaced one meter apart to collect individual trajectories. Following and leading vehicle trajectories were then linked, resulting in 77 pairs of vehicles. Guido et al. verified the values they estimated for vehicle speeds by measuring speeds with laser guns and comparing the results. Laser guns were set up at six reference stations, including four stations at the roundabout entrances/exits. A statistical analysis of the speeds calculated from the video footage and the speeds measured using the laser guns revealed that no statistically significant difference existed between the two methods of measuring vehicle speed.

The paper next detailed the computation of SSMs from the 77 identified interactions. For CPI, two values were used for the MADR. The first definition was based on the coefficient of friction and cross grade of the pavement. The second definition was based on a truncated normal distribution with a minimum value of 4.2 m/s^2 and a maximum value of 12.7 m/s^2. Potential conflicts were defined as interactions with a DRAC exceeding 3.35 m/s^2, a TTC lower than 1.5 seconds, a PSD less than or equal to 1, a TIT greater than zero, or a CPI greater than zero. Guido et al. used a standardized U-statistic to compare the safety measures. This statistic was calculated using Equation 12:

$$u = \frac{x - x_{\min}}{x_{\max} - x_{\min}} \quad (12)$$

where, x is the observed exposure time to a conflict value, x_{min} is the minimum observed exposure time to a conflict value, and x_{max} is the maximum observed exposure time to a conflict value.

The paper concluded with a discussion of the characteristics of the SSMs that were highlighted in the study. Guido et al. found very similar results with TIT and TTC in the safety analysis. PSD resulted in a higher time exposure to hazardous situations and nebulous results as to where safety problems existed. Guido et al. also found similar results for both of the CPI measures, although the CPI using the distributed MADR led to more localized results. Relative to other measures, CPI underestimated risk possibly, due to CPI's consideration of braking capacity. The measures all identified areas with significant merging activity. This exposes vehicles to more abrupt acceleration and deceleration rates as well as traffic flow turbulence. Overall, the study revealed that measures that require a larger number of inputs, such as CPI, yielded more focused results regarding locations of safety hazards. These more focused results may potentially be of greater use to decision-makers in determining which safety improvements ought to be prioritized.

Paper #5:
Comparing Simulated Road Safety Performance to Observed Crash Frequency at Signalized Intersections

This paper, written by Souza, Sasaki, and Cunto (2011), was submitted to the International Conference on Road Safety and Simulation. The paper details a study in which the researchers conducted one of the validation efforts suggested in the FHWA report, namely validation by correlating SSMs and traditionally gathered crash data. The authors of that study considered intersections in Fortaleza,

Brazil, and a comparison of simulation results with real-world data was done for both peak and off-peak two-hour periods. The SSMs evaluated in the paper included TTC, DRAC, and CPI. The number of rear-end collisions was observed to decrease over a period of approximately three years (2007, 2008, and 2009), but the SSMs, as computed with microsimulation programs, did not reflect this decrease (Souza, Sasaki, & Cunto, 2011).

Souza et al. (2011) stated that SSMs fall into three categories: time-based measures, measures of required braking power, and safety indices. All of these categories serve to provide a proactive approach to safety analysis. Another benefit of SSMs over crash data is the significantly greater frequency of high-risk situations in comparison to crashes, which means that statistical methods are more reliable. Souza et al. pointed out a limitation in time-based measures in that multiple scenarios may result in the same value. For instance, a low speed at a close following distance may have the same TTC as a high speed at a longer following distance. This makes it difficult to use time-based measures effectively to determine crash severity. For this reason, measures of required braking power and safety indices can be more useful. Souza et al. considered one measure from each category (TTC, DRAC, and CPI) then used the geometric and traffic characteristics of three intersections to build six scenarios in PTV VISSIM: peak and off-peak models for each of the three intersections.

The results of the simulation included the number of conflicts over a three-year period and the number of conflicts per vehicle over a three-year period. The results were for three years so that they could be compared to crash data from the same period. The crash data exhibited a downward trend over the three-year timespan, which was not predicted by the SSMs. Souza et al. suggested that the simulation environment's simplicity and the rareness of collisions may have accounted for this discrepancy. The TTC and DRAC measures resulted in a much higher number of conflicts than did CPI. CPI also exhibited the highest variability, which was due to the inclusion of two stochastic components: random seed generation and a distribution of maximum available deceleration rates. Crashes and conflicts increase with increased traffic volume, and the three-approach intersection in the study had significantly fewer conflicts and collisions than the other two intersections with four approaches. This supports the idea that increased exposure increases conflict and crash numbers (Souza et al., 2011).

The paper concluded with ideas regarding the correlation of the SSMs with actual crash data. In spite of the microsimulation not capturing the downward trend in collisions, the SSMs did find the differences in the numbers of crashes at each of the three intersections considered. This suggests that microsimulations may be used for proactive safety analysis. Souza et al. (2011) suggested further research in incorporating parking maneuvers in safety analyses and including more types of vehicles, such as motorcycles that were excluded from the study. Another potential research area is the use of safety performance models to improve crash estimates.

Paper #6:
Use of Crash Surrogates and Exceedance Statistics to Estimate Road Safety

In this article, Tarko (2012) presents a new type of safety model that is a combination of multiple previous safety models but which expands the narrow abilities of existing models. Tarko writes that the narrow abilities of prior models are due to the use of poor-quality data to estimate complicated safety factors. Data quality has improved because of better sensing techniques and technology and naturalistic driving data collection. The new model presented in this article improves upon past techniques by including crash precursor events into an estimation method that makes use of the Generalized Pareto distribution.

The paper begins with an overview of past methods for determining what events should be classified as traffic conflicts. Tarko explains that a pyramid may be used as a representation of the frequency of traffic interactions, based on their riskiness level and includes a diagram showing such a pyramid. It is broken into sections representing, in order of increasing riskiness level, undisturbed passages, potential traffic conflicts, light traffic conflicts, serious traffic conflicts, and collisions. Less risky interactions comprise larger portions of the total volume of the pyramid than riskier interactions, indicating the higher frequency of less risky interactions (Tarko, 2012). The author then proposes an approach to developing a better model for traffic interactions by defining the number, n, of traffic interaction classes. The assumptions for this model are that interaction severity is continuous, an event belongs to a particular interaction class if its severity is above a particular threshold, and the distribution of the severity of events has a right tail that converges to zero. Collision proximity, in turn, may be determined by finding the difference between event severity and the collision severity threshold.

Tarko goes on to explain that the model is an exceedance distribution that may be used in conjunction with the Extreme Value Theory. An equivalent form of the generalized extreme values distribution is the Generalized Pareto distribution, which is applicable to values in exceedance of a large, fixed threshold. This distribution, and the Extreme Value Theory in general, has been used in areas concerning safety analysis, such as natural disasters, financial losses, and engineering failures. According to Tarko, the generalized extreme values and Generalized Pareto distributions can be used to estimate how frequently a car will depart from a roadway. The riskiness of events is broken into the following categories: all events, risky events, and actual road departures, which may or may not be crashes. A fourth category, representing crashes following road departure, may be incorporated into a complete safety model.

Tarko defines a number of terms, including threshold, risky event range, and event severity. The threshold of a risky event is the lateral clearance below which a driver would feel uncomfortable. The risky event range is the longitudinal distance over which a vehicle is too close to the edge of the road and signifies the distance required for a driver to become uncomfortable and make a corrective motion. Event severity is the proximity of a risky event to an actual road departure and is useful for fitting the Generalized Pareto distribution.

The article outlines experiments conducted with a driving simulator and four test drivers. The track in the simulator featured many horizontal curves as well as accurate signage, billboards, a realistic rural background landscape, and traffic flowing in the same direction as the driver. The test subjects drove 2052 miles, departing the road four times and experiencing 2500 risky events. Using the bootstrap method, Tarko found ninety percent confidence intervals for road departures based on the number of risky events. The actual number of road departures was not used in the determination of these confidence intervals but did fall within the interval, which gives credence to the intervals and the methods used to find them.

Tarko developed models for the probabilities of risky events, crashes, and crash severity as well as a model that computes the frequency of collisions of varying severity levels. Tarko's models were SSMs, taking data other than crash data and producing crash count and risky event count estimates. The consideration of the breakdown of collision severity is a valuable contribution to the literature on SSMs. Tarko called for subsequent research into application of Pareto models to suitable data. Pareto models could potentially be used in conjunction with connected vehicle data or data from microsimulation software to determine the expected crash frequency along roadways.

Paper #7:
Surrogate Safety Measure for a Simulation-Based Conflict Study

In this paper, Wang and Stamatiadis (2013) outlined the development of an SSM called the aggregated crash propensity metric (ACPM) that can be used with microsimulation software programs to evaluate intersection safety. Wang and Stamatiadis also described a probabilistic model that was developed to incorporate the distributions of driver reaction times and deceleration rates during braking. This serves to compute the probability of crashes that fit into three categories: rear-end, crossing, and lane change. The measure was validated using VISSIM models and it was found that the ACPM performed better than the Highway Safety Manual methods in determining the relative safety of intersection designs. Attempts to correlate ACPM with real crash data was in its early stages at the time this paper was published, but the early findings suggest the potential for ACPM to be used to predict actual crash numbers.

In the article, the authors begin with a discussion of SSMs and the apparent need for a new metric that more fully utilizes the detailed data produced by microsimulations. According to the authors, SSMs have not grown in complexity sufficiently with advancements in microsimulation. The SSAM, for instance, uses TTC with an arbitrary threshold of 1.5 seconds to measure safety. Wang and Stamatiadis intended to bridge the gap with the ACPM. The ACPM measures the probability for each conflict at an intersection to result in a collision, while considering human and vehicular variations. For every conflict, there exists a portion of the driver population that has a reaction time longer than the TTC, and there exists a portion of vehicles that have a maximum available braking rate that is lower than the required braking rate. The reaction time distribution is a lognormal distribution with parameters that depend on the type of collision (crossing, lane-change, and rear-end). The maximum available braking rate distribution is a truncated normal distribution with a mean of 9.7 m/s^2, a standard deviation of 1.3 m/s^2, a lower limit of 4.2 m/s^2, and an upper limit of 12.7 m/s^2, as determined in prior research (Wang & Stamatiadis, 2013).

Wang and Stamatiadis presented graphs of the probability density functions of these distributions in their paper. Both of the graphs were divided into two parts by a vertical dividing line. The vertical dividing line in the reaction time distribution was the TTC, and the vertical dividing line in the maximum available braking rate distribution was the required braking rate. In the reaction time distribution, the area under the curve to the right of the dividing line was labeled "Group A," and the area under the curve to the left was labeled "Group B." In the maximum available braking rate distribution, the area under the curve to the right of the dividing line was labeled "Group B-1," and the area under the curve to the left was labeled "Group B-2" (Wang & Stamatiadis, 2013). The groups created by the graphs were used to determine the crash propensity metric and, ultimately, the ACPM. Drivers in group A did not react in time to avoid a collision. Drivers in group B-2 reacted quickly enough to initiate an evasive maneuver, but were unable to perform the evasive maneuver successfully, due to vehicular limitations. The sum of these groups (A and B-2) were all the conflicts that would result in a collision. The probability of a collision for an individual conflict was the crash propensity metric, and the sum of all propensity metrics for conflicts within a particular category was the ACPM (Wang & Stamatiadis, 2013).

The required braking rate was derived for each of the three types of collisions using kinematics. Wang and Stamatiadis derived equations, where l_i and w_i are the length and width of vehicle i, V_i is the velocity of vehicle i, D is the distance between conflicting vehicles, θ is the conflict angle, and x is the reaction time. Equations 13 and 14 are for crossing conflicts. Equation 13 calculates the total time t during which the leading vehicle is at the conflict point. Equation 14 finds the required braking rate for a crossing

conflict and uses the output of Equation 13. For rear-end conflicts, Equation 15 can be used to find the required braking rate, and, for lane change conflicts, Equation 16 can be used to find the required braking rate.

$$t = \frac{l_1 + \frac{w_1}{\tan\theta} + \frac{w_2}{\sin\theta}}{V_1} \tag{13}$$

$$RBR(\text{crossing}) = \frac{V_2 * t}{\left(TTC + \frac{t}{2} - x\right)^2} \tag{14}$$

$$RBR(\text{rear end}) = \frac{(V_2 - V_1)}{2 * (TTC - x)} \tag{15}$$

$$RBR(\text{lane change}) = \frac{\frac{2V_2 l_1}{V_1} + l_2 - l_1 * \cos\theta - \frac{w_1}{\sin\theta} - \frac{w_2}{\tan\theta}}{\left(TTC + \left(\frac{l_1}{V_1}\right) - x\right)^2} \tag{16}$$

The crash propensity metric illuminates the differences between two scenarios that may appear identical when looking only at the TTC. In two scenarios with an identical TTC, the required braking rates, however, may be quite different. This makes one scenario more likely to result in a collision, and the crash propensity metric will indicate just how much more likely it is (Wang & Stamatiadis, 2013).

Wang and Stamatiadis validated the ACPM using experimentation with VISSIM models of twelve intersections on three arterials in Kentucky. The ACPM was computed for each of the three collision types at all of the intersections. The total ACPM is the sum of the three collision type-specific ACPM values. The researchers ranked the intersections according to their relative safety and the ACPM and then predicted the annual numbers of crashes at each of the intersections using the methods presented in the Highway Safety Manual. Spearman rank tests showed high rank correlation coefficients, indicating that the ACPM is a good indicator of relative intersection safety. The researchers also used the leave-one-out cross-validation method to test the ability of the ACPM to predict crash numbers at each of the intersections. The actual crash numbers fell within the 95% confidence interval of the crash predictions most of the time, indicating that ACPM is promising for use as a crash predictor.

Wang and Stamatiadis concluded the paper by reiterating that the ACPM is an SSM to be used for determining the relative safety of transportation infrastructure. The metric successfully determines the probability of crashes using TTC without an arbitrary cutoff value, a weakness of the previous use of TTC. Wang and Stamatiadis pointed out that VISSIM's simulation operates based on the assumption that all drivers will follow the rules regarding right-of-way. Of course, this is not always the case and may lead to crossing conflicts being underrepresented. Practitioners may benefit from using another method to characterize crossing conflicts.

Paper #8:
Identifying High Crash-Risk Roadways Through Jerk-Cluster Analysis

In this paper—a thesis written by Mousavi (2015) and submitted to the Louisiana State University as part of the requirements for a master's degree—the author details a study that used naturalistic driving data from GPS sensors to identify locations in which high concentrations of abnormal driving events occur and correlate crash rates to these abnormal events. These events involved sudden and unusual movements of vehicles that could be detected through a measurement of the vehicle's first derivative of acceleration, known as jerk. Mousavi noted the importance of the work as a means of computing estimates for crash occurrence without crashes actually having to occur in order to produce data. This is in contrast to the standard methods of safety analysis that are retroactive in nature, relying on long-term historic crash data to identify locations that are less safe than others for the purposes of prioritizing improvements.

Mousavi (2015) explained the methodology conducted in the research. Data collection was done through the use of GPS to generate naturalistic driving data. GPS units were placed in 31 study participants' vehicles. The GPS data were filtered to remove erroneous data points. These errors included noise, wandering, and gaps in the GPS data. Noise was the most prevalent error and included clusters of points around intersections, where vehicles were moving slowly. Wandering occurred when GPS points appeared in locations where no road existed and were seemingly random. Gaps were places along roadways where data points were missing, due to loss of signal between the GPS units and satellites. These errors were removed with the use of the Savitzky-Golay filter (Mousavi, 2015).

The next step in the methodology was differentiating the vehicles' velocity values twice in order to obtain jerk values. Because data were collected at discrete time intervals, jerks were computed for each interval. Because the research in this study was intended to conduct a microscale analysis, the roadways were segmented to obtain smaller study areas. Three different scales were tested: eighth-mile, quarter-mile, and half-mile segments. These segment lengths played a role in the calculation of road segment crash rates for each of the segments. This rate, expressed for 100 million vehicle-miles, was calculated using Equation 17 from the U.S. Department of Transportation (Mousavi, 2015):

$$R = \frac{C \times 100,000,000}{V \times 365 \times N \times L} \quad (17)$$

where, C is the number of crashes on a segment, V is the average daily traffic (ADT) on the segment, N is the number of years of crash data, and L is the road segment length.

Input values for this equation were obtained in order to calculate the segment crash rates. Crash counts were obtained for a 5-year period between the beginning of 2009 and the end of 2013. There were 1352 crashes on LA 1248 and 1188 crashes on LA 42. The segment length varied between eighth-mile, quarter-mile, and half-mile segments, depending upon the scale being tested. The ADT for each segment was computed by using data from the Louisiana Department of Transportation and the Inverse Distance Weighted interpolation tool within GIS software. With these input values, the crash rates could be calculated (Mousavi, 2015).

Mousavi discussed a sensitivity analysis that was done to determine the proper jerk value to use as a threshold between normal and abnormal events. Because there was no clear threshold value to use for a continuous variable such as jerk, a data-driven sensitivity analysis determined the best threshold value to use from a selection of test values. Threshold values tested began at -0.5 ft/s^3 and decreased in increments of 0.5 ft/s^3 until a final test threshold value of -10.5 ft/s^3 was reached. A count of the number of abnormal events was then obtained and normalized based upon the total number of data points to obtain a jerk ratio for each of the segments. Again, three segment lengths were considered for both of the roadways included in the study. Pearson's correlation coefficients were computed and revealed that a jerk threshold of -2.5 ft/s^3 and a segment length of one -quarter mile were most highly correlated with crash counts (Mousavi, 2015).

The next part of the analysis was crash frequency modeling. Two crash frequency models were created for each of the roads studied, resulting in four total models. The first type of model created included only the jerk ratio as an independent variable. The second type of model included both the jerk ratio and the presence of horizontal curvature as explanatory variables. Negative binomial regression was used to create all four models. Crash frequency modeling found that the jerk ratio was highly significant and possessed a positive correlation with crash rate. In contrast, the presence of curvature was only significant for one of the roads (LA 42) at a 95% level of significance. Therefore, presence of curvature was not established as a meaningful predictor of crash occurrence. The value of the coefficient for the presence of curvature variable was computed to be negative, indicating that the presence of curvature tends to decrease the number of crashes that occur. This suggests that drivers adjust their behavior to drive more cautiously when curves are present, thereby leading to fewer crashes (Mousavi, 2015).

The thesis concluded with a discussion of the limitations of the methodology and ideas for future research. Mousavi stated that the GPS data were of low quality and low frequency. To capture braking information requires a high sampling rate. This problem may potentially be solved with the use of connected vehicle data. Additionally, the ADT values were interpolated using the Inverse Distance Weighted interpolation tool. This is a powerful tool, but it is possible that the interpolated values for ADT were not accurate. Having actual ADT counts would lead to a more accurate analysis. Mousavi called for further research into the ideal segment length for jerk-cluster safety analysis with the use of a spatial analysis tool and suggested that detailed curve information, such as sharpness and radius, be included as explanatory variables in future safety models.

Paper #9:
Assessing Surrogate Safety Measures Using a Safety Pilot Model Deployment Dataset

In this 2018 article by He, Qin, Liu, and Sayed, the authors detailed a study in which SSMs were used in conjunction with data collected by the Safety Pilot Model Deployment (SPMD) program in Ann Arbor, Michigan. The SPMD program used connected vehicles and thirty items of roadside equipment to collect a variety of types of data on the vehicles involved in the program. He, Qin, Liu, and Sayed used the kinematic data to evaluate the risk of mid-block rear-end crashes using SSMs. The authors also used three different measures: TTC, modified TTC (MTTC), and DRAC. The difference between TTC and MTTC is the inclusion of acceleration in MTTC. TTC is based on the assumption of a constant vehicle speed, but MTTC allows for acceleration or deceleration to be considered. These measures were used as a safety index to determine the level of danger present on various links in Ann Arbor. The measures were then compared to actual crash data to determine the goodness of fit, using a statistical analysis with negative binomial regression. This statistical analysis revealed that the MTTC was the best of the SSMs (He et al., 2018).

He et al. included the equations they used to calculate the SSMs. These equations can be incorporated into other research that uses connected vehicle data. He et al. also presented a map with the locations of crashes, indicated as points and the safety index shown along links in the roadway network. Similar maps can be generated by other researchers using various GIS software programs such as ArcGIS. This could be a valuable addition to a study that investigates harsh braking events such as SSMs. He et al. ended the paper with some suggestions for future research. One area in which researchers could build upon this study is in the data processing approach. He et al. acknowledged that their method of data processing may not have been ideal, due to some of the assumptions made, and called for research into finding other effective approaches as well as incorporating additional SSMs, such as PET and the differ-

ence in vehicle velocities. They also suggested that future research take place regarding the use of signal phasing and timing (SPaT) data. This research could potentially illuminate relationships between red-light running and safety (He et al., 2018).

Paper #10:
Surrogate Safety Measures from Traffic Simulation—Validation of Safety Indicators with Intersection Traffic Crash Data

In this final paper (Astarita et al., 2020), the authors propose and validate a new SSM. This new measure uses vehicle trajectories and the mean energy of a vehicle to determine a safety metric and is capable of considering the dangers of single-vehicle crashes into roadside objects. These considerations have not been incorporated in SSMs prior to this paper. The researchers validated their new metric by comparing its results to both historical data and measures produced by other means, such as TTC and PET. Astarita et al. began by reviewing the published literature on SSMs and highlighting concerns with the existing measures. They described measures such as TTC, PET, and DRAC. They also described a new traffic microsimulation program called TRITONE that evaluates road safety and has been validated through comparison with the SSAM. Astarita et al. listed four topics that caused concern with the existing measures: human factor modeling, traffic simulation packages, traffic safety indicators, and friction and shear forces in traffic flows.

In the article, the authors went on to describe the their reasoning behind each of the concerns. In terms of human factor modeling, the prior measures did not consider human error or human distraction. These are usually caused by drivers multitasking and account for approximately 30% of crashes in the U.S. In considering traffic simulation packages, the authors raised concerns about the inability of most programs to compute SSMs as well as the SSAM's inability to characterize crash severity or map locations of conflicts. In terms of traffic safety indicators, they pointed out that SSMs do not consider the outcome of a traffic conflict, should it become a collision. Finally, they expressed concerns over the lack of consideration for potential conflicts between vehicles that are on trajectories and which do not intersect vehicles and roadside objects.

With these concerns in mind, the researchers described how their new SSM would address these lacunae. Beginning with a starting dataset for vehicle trajectories within a network, the researchers extracted both the position and speed for every single vehicle in the dataset for every second of their simulation. For each of these vehicle speeds and locations, the researchers calculated deviated trajectories that occupied a particular angle to the right or to the left of the vehicle's neutral trajectory along the road. The angle was generated with a Gaussian distribution. The deviated trajectories were then followed by the vehicle for a particular distraction time, which the researchers assumed to be five seconds. With these distracted paths calculated for the vehicles, potential collisions with other vehicles or roadside objects were determined, and the energy of impact in the crash was calculated using the physics of inelastic collisions (Astarita et al., 2020).

This methodology solved the concerns of the researchers in a number of ways. First, it takes human error and distraction into account through the deviated courses. This allows for conflicts between vehicles on paths that do not overlap to be considered, such as conflicts between vehicles traveling in opposite directions along a roadway. This also allows for single-vehicle crashes to be represented, as long as the location, shape, and material properties of roadside objects are included in the analysis. Finally, the crash dynamics are represented in the simulation, which means that impact energy is known. The researchers ran their simulation using TRITONE for four scenarios involving nine intersections in Salerno, Italy. The results of the simulations included numbers of crashes and mean collision energy. For comparison, the researchers also computed numbers of collisions from TTC and PET with threshold values (Astarita et al., 2020).

With these results, the authors detailed a statistical analysis of the two methods of estimating crash counts. This analysis involved the computation of the root mean square error and likelihood ratio test statistic for each method. The researchers developed two models, Model A and Model B. Model A uses TTC, PET, traffic flow, and a dummy variable as explanatory variables. Model B uses mean collision energy, traffic flow, and a dummy variable as explanatory variables. The statistical analysis demonstrated that both of these models were statistically equivalent and Model B was able to estimate crash counts accurately, as evidenced by a comparison to five-year crash counts. The findings of this paper suggest that crash counts may be successfully estimated using trajectory deviations to calculate mean collision energy and then fitting a model with that as an explanatory variable. Astarita et al. noted that their simulations made use of many default values for parameters, so they recommend further research into ways to calibrate this methodology to a specific area.

Discussion

Practitioners may apply the findings of the papers considered here to conduct a variety of types of surrogate safety analyses that vary in both the measures used and the ways in which data are collected for the analyses. SSMs include time-based measures, deceleration-based measures, and safety indices. Time-based measures include TTC, TET, TIT, PET, IAPE, and PSD. Deceleration-based measures include DRAC and the use of harsh braking data, as indicated by the jerk values experienced by vehicles. Safety indices include CPI and ACPM. The method used by Astarita et al. involved developing a crash prediction equation that

used a combination of time-based measures and traffic flow characteristics. Although it is possible to collect data for SSMs with in-person observations or video data, the standard methods at this point in time include simulation with VISSIM or TRITONE models or use of connected vehicle data. Additional processing is necessary for both of these methods.

In order for practitioners to conduct surrogate safety analysis, they must first collect data on the intersection or link being considered. If using microsimulations, such data would include the roadway geometry and traffic characteristics. Analysis with simulation involves building models in VISSIM, TRITONE, or another suitable microsimulation program and then processing the output kinematic data with the Federal Highway Administration's SSAM. The equations presented throughout this paper may also be used with such kinematic data to compute SSMs. Connected vehicle data are currently available through vendors but may eventually be available to the public in the future. Practitioners can use the kinematic data from connected vehicles as inputs to the SSM equations included throughout this paper, as was done by He et al. (2018). Simulation and connected vehicle data allow for proactive safety analysis and preemptive safety improvements.

These papers vary in their levels of usefulness at this point in time. Newer papers, of course, have an advantage over older papers, due to their authors having the benefit of a greater amount of prior research. However, some older papers, such as Allen et al.'s 1978 paper, still offer useful insights and SSMs. Table 1 is a rubric of the usefulness of the papers considered here with different categories that may concern practitioners looking into implementing their methods.

Table 1. Rubric of usefulness for papers considered.

Paper Number - Year	Theoretical Value	Practical Value	Relevance	Difficulty of Implementation
1 – 1978	Most	Most	Medium	Medium
2 – 2001	Medium	Medium	Medium	Medium
3 – 2003	Least	Most	Medium	Least Difficult
4 – 2010	Most	Least	Least	Most Difficult
5 – 2011	Least	Medium	Medium	Least Difficult
6 – 2012	Most	Least	Least	Most Difficult
7 – 2013	Most	Medium	Most	Medium
8 – 2015	Medium	Most	Most	Least Difficult
9 – 2018	Medium	Most	Most	Medium
10 - 2020	Most	Medium	Most	Most Difficult

Conclusions

Traffic safety analyses with surrogate safety measures have evolved over the past several decades both in terms of the measures themselves and in the technology used to compute them. The articles and reports summarized in this paper range in publication year between 1978 and 2020, illustrating this evolution. The earliest method of computing surrogate safety measures was the use of time-lapse imagery, which eventually gave way to microsimulation and, more recently, the implementation of connected vehicle data. Use of microsimulation greatly improved the precision with which surrogate safety measures could be computed, but was also an abstraction. Connected vehicle data supply both the realism of on-site measurement and the precision that is available with microsimulation, making it the preferred technology at this point in time. The measures have evolved from simply counting brake applications to taking kinematics into account or measuring rates of deceleration to determine where safety hazards exist. Surrogate safety measures represent a means of preventing crashes and the damages, injuries, and loss of life that crashes cause. Research on surrogate safety measures has made great strides, as demonstrated by the articles considered in this paper. Continuing research into making these methods more easily implemented and more effective through the use of connected vehicle data could lead to much more effective safety analyses, more targeted infrastructure improvements, and safer roads and intersections for the public.

References

Allen, B. L., Shin, B. T., & Cooper, D. J. (1978). Analysis of Traffic Conflicts and Collisions. *Transportation Research Record, 667*, 67-74. http://onlinepubs.trb.org/Onlinepubs/trr/1978/667/667-009.pdf

Astarita, V., Caliendo, C., Giofré, V. P., & Russo, I. (2020). Surrogate Safety Measures from Traffic Simulation: Validation of Safety Indicators with Intersection Traffic Crash Data. *Sustainability*, *6974*(12), 1-20. https://doi.org/10.3390/su12176974

Gettman, D., & Head, L. (2003). *Surrogate Safety Measures from Traffic Simulation Models Final Report*. U.S. Department of Transportation Federal Highway Administration Office of Research, Development, and Technology. https://doi.org/10.3141/1840-12

Guido, G., Saccomanno, F., Vitale, A., Astarita, V., & Festa, D. (2010). Comparing Safety Performance Measures Obtained from Video Capture Data. *Journal of Transportation Engineering, 137*(7), 481-491. http://dx.doi.org/10.1061/(ASCE)TE.1943-5436.0000230

He, Z., Qin, X., Liu, P., & Sayed, M. A. (2018). Assessing Surrogate Safety Measures Using a Safety Pilot Model Deployment Dataset. *Transportation Research Record*, *2672*(38), 1-11. https://doi.org/10.1177/0361198118790861

Minderhoud, M. M., & Bovy, P. H. (2001). Extended Time-to-Collision Measures for Road Traffic Safety Assessment. *Accident Analysis and Prevention, 33*(1), 89-97. https://doi.org/10.1016/S0001-4575(00)00019-1

Mousavi, S. M. (2015). *Identifying High Crash Risk Roadways through Jerk-Cluster Analysis* (Master's thesis, Louisiana State University). https://digitalcommons.lsu.edu/gradschool_theses/159

Souza, J. Q., Sasaki, M. W., & Cunto, F. J. C. (2011, September 14-16). *Comparing Simulated Road Safety Performance to Observed Crash Frequency at Signalized Intersections*. Paper presented at the International Conference on Road Safety and Simulation. http://onlinepubs.trb.org/onlinepubs/conferences/2011/RSS/2/Souza,J.pdf

Tarko, A. P. (2012). Use of Crash Surrogates and Exceedance Statistics to Estimate Road Safety. *Accident Analysis and Prevention*, *45*, 230-240. https://doi.org/10.1016/j.aap.2011.07.008

Wang, C., & Stamatiadis, N. (2013). Surrogate Safety Measure for Simulation-Based Conflict Study. *Transportation Research Record*, *2386*, 72-80. https://doi.org/10.3141/2386-09

Biographies

NATHANIEL EDELMANN is a graduate student pursuing a Master of Science degree in Civil Engineering at Boise State University. He earned his BS in civil engineering from Boise State University in 2020. Mr. Edelmann's thesis research concerns traffic safety analysis through the use of surrogate safety measures. Mr. Edelmann may be reached at nathanieledelmann@u.boisestate.edu

MANDAR KHANAL is a professor of civil engineering at Boise State University. Dr. Khanal earned his MS degree from Northwestern University and PhD from the University of California, Irvine. He is a registered civil engineer in California and Idaho. At Boise State University, Dr. Khanal is responsible for the Transportation Engineering program and continuously developing new courses within this field. He is also involved in many research projects funded by state and federal agencies. Dr. Khanal may be reached at mkhanal@boisestate.edu

INSTRUCTIONS FOR AUTHORS: MANUSCRIPT FORMATTING REQUIREMENTS

The INTERNATIONAL JOURNAL OF MODERN ENGINEERING is an online/print publication designed for Engineering, Engineering Technology, and Industrial Technology professionals. All submissions to this journal, submission of manuscripts, peer-reviews of submitted documents, requested editing changes, notification of acceptance or rejection, and final publication of accepted manuscripts will be handled electronically. The only exception is the submission of separate high-quality image files that are too large to send electronically.

All manuscript submissions must be prepared in Microsoft Word (.doc or .docx) and contain all figures, images and/or pictures embedded where you want them and appropriately captioned. Also included here is a summary of the formatting instructions. You should, however, review the sample Word document on our website (http://ijme.us/formatting_guidelines/) for details on how to correctly format your manuscript. The editorial staff reserves the right to edit and reformat any submitted document in order to meet publication standards of the journal.

The references included in the References section of your manuscript must follow APA-formatting guidelines. In order to help you, the sample Word document also includes numerous examples of how to format a variety of scenarios. Keep in mind that an incorrectly formatted manuscript will be returned to you, a delay that may cause it (if accepted) to be moved to a subsequent issue of the journal.

1. **Word Document Page Setup:** Two columns with ¼" spacing between columns; top of page = ¾"; bottom of page = 1" (from the top of the footer to bottom of page); left margin = ¾"; right margin = ¾".

2. **Paper Title:** Centered at the top of the first page with a 22-point Times New Roman (Bold), small-caps font.

3. **Page Breaks:** Do not use page breaks.

4. **Figures, Tables, and Equations:** All figures, tables, and equations must be placed immediately after the first paragraph in which they are introduced. And, each must be introduced. For example: "Figure 1 shows the operation of supercapacitors." "The speed of light can be determined using Equation 4:"

5. **More on Tables and Figures:** Center table captions above each table; center figure captions below each figure. Use 9-point Times New Roman (TNR) font. Italicize the words for table and figure, as well as their respective numbers; the remaining information in the caption is not italicized and followed by a period—e.g., "*Table 1*. Number of research universities in the state." or "*Figure 5*. Cross-sectional aerial map of the forested area."

6. **Figures with Multiple Images:** If any given figure includes multiple images, do NOT group them; they must be placed individually and have individual minor captions using, "(a)" "(b)" etc. Again, use 9-point TNR.

7. **Equations:** Each equation must be numbered, placed in numerical order within the document, and introduced—as noted in item #4.

8. **Tables, Graphs, and Flowcharts:** All tables, graphs, and flowcharts must be created directly in Word; tables must be enclosed on all sides. The use of color and/or highlighting is acceptable and encouraged, if it provides clarity for the reader.

9. **Textboxes:** Do not use text boxes anywhere in the document. For example, table/figure captions must be regular text and not attached in any way to their tables or images.

10. **Body Fonts:** Use 10-point TNR for body text throughout (1/8" paragraph indention); indent all new paragraphs as per the images shown below; do not use tabs anywhere in the document; 9-point TNR for author names/affiliations under the paper title; 16-point TNR for major section titles; 14-point TNR for minor section titles.

11. **Personal Pronouns:** Do not use personal pronouns (e.g., "we" "our" etc.).

12. **Section Numbering:** Do not use section numbering of any kind.

13. **Headers and Footers:** Do not use either.

14. **References in the Abstract:** Do NOT include any references in the Abstract.

15. **In-Text Referencing:** For the first occurrence of a given reference, list all authors—last names only—up to seven (7); if more than seven, use "et al." after the seventh author. For a second citation of the same reference—assuming that it has three or more authors—add "et al." after the third author. Again, see the *sample Word document* and the *formatting guide for references* for specifics.

16. **More on In-Text References:** If you include a reference on any table, figure, or equation that was not created or originally published by one or more authors on your manuscript, you may not republish it without the expressed, written consent of the publishing author(s). The same holds true for name-brand products.

17. **End-of-Document References Section:** List all references in alphabetical order using the last name of the first author—last name first, followed by a comma and the author's initials. Do not use retrieval dates for websites.

18. **Author Biographies:** Include biographies and current email addresses for each author at the end of the document.

19. **Page Limit:** Manuscripts should not be more than 15 pages (single-spaced, 2-column format, 10-point TNR font).

20. **Page Numbering:** Do not use page numbers.

21. **Publication Charges:** Manuscripts accepted for publication are subject to mandatory publication charges.

22. **Copyright Agreement:** A copyright transfer agreement form must be signed by all authors on a given manuscript and submitted by the corresponding author before that manuscript will be published. Two versions of the form will be sent with your manuscript's acceptance email.

    Only one form is required. Do not submit both forms!

    The form named "paper" must be hand-signed by each author. The other form, "electronic," does not require hand signatures and may be filled out by the corresponding author, as long as he/she receives written permission from all authors to have him/her sign on their behalf.

23. **Submissions:** All manuscripts and required files and forms must be submitted electronically to Dr. Philip D. Weinsier, manuscript editor, at philipw@bgsu.edu.

24. **Published Deadlines:** Manuscripts may be submitted at any time during the year, irrespective of published deadlines, and the editor will automatically have your manuscript reviewed for the next-available issue of the journal. Published deadlines are intended as "target" dates for submitting new manuscripts as well as revised documents. Assuming that all other submission conditions have been met, and that there is space available in the associated issue, your manuscript will be published in that issue if the submission process—including payment of publication fees—has been completed by the posted deadline for that issue.

    Missing a deadline generally only means that your manuscript may be held for a subsequent issue of the journal. However, conditions exist under which a given manuscript may be rejected. Always check with the editor to be sure. Also, if you do not complete the submission process (including all required revisions) within 12 months of the original submission of your manuscript, your manuscript may be rejected or it may have to begin the entire review process anew.

CUTTING EDGE JOURNAL OF RESEARCH AND INNOVATION IN ENGINEERING

Print ISSN: 2152-4157
Online ISSN: 2152-4165

www.ijeri.org

www.iajc.org

INTERNATIONAL JOURNAL OF ENGINEERING RESEARCH AND INNOVATION

ABOUT IJERI:

- IJERI is the second official journal of the International Association of Journals and Conferences (IAJC).
- IJERI is a high-quality, independent journal steered by a distinguished board of directors and supported by an international review board representing many well-known universities, colleges, and corporations in the U.S. and abroad.
- IJERI has an impact factor of **1.58**, placing it among an elite group of most-cited engineering journals worldwide.

OTHER IAJC JOURNALS:

- The International Journal of Modern Engineering (IJME) For more information visit www.ijme.us
- The Technology Interface International Journal (TIIJ) For more information visit www.tiij.org

IJERI SUBMISSIONS:

- Manuscripts should be sent electronically to the manuscript editor, Dr. Philip Weinsier, at philipw@bgsu.edu.

  For submission guidelines visit www.ijeri.org/submissions

TO JOIN THE REVIEW BOARD:

- Contact the chair of the International Review Board, Dr. Philip Weinsier, at philipw@bgsu.edu.

  For more information visit www.ijeri.org/editorial

INDEXING ORGANIZATIONS:

- IJERI is currently indexed by 16 agencies. For a complete listing, please visit us at www.ijeri.org.

Contact us:

Mark Rajai, Ph.D.

Editor-in-Chief
California State University-Northridge
College of Engineering and Computer Science
Room: JD 4510
Northridge, CA 91330
Office: (818) 677-5003
Email: mrajai@csun.edu

www.tiij.org

www.ijme.us

THE LEADING JOURNAL OF ENGINEERING, APPLIED SCIENCE AND TECHNOLOGY

The latest impact factor (IF) calculation (Google Scholar method) for IJME of 3.0 moves it even higher in its march towards the top 10 engineering journals.

IJME IS THE OFFICAL AND FLAGSHIP JOURNAL OF THE INTERNATIONAL ASSOCATION OF JOURNALS AND CONFERENCE (IAJC)
www.iajc.org

The International Journal of Modern Engineering (IJME) is a highly-selective, peer-reviewed journal covering topics that appeal to a broad readership of various branches of engineering and related technologies. IJME is steered by the IAJC distinguished board of directors and is supported by an international review board consisting of prominent individuals representing many well-known universities, colleges, and corporations in the United States and abroad.

IJME Contact Information

General questions or inquiries about sponsorship of the journal should be directed to:

Mark Rajai, Ph.D.
Editor-in-Chief
Office: (818) 677-5003
Email: editor@ijme.us
Department of Manufacturing Systems Engineering & Management
California State University-Northridge
18111 Nordhoff St.
Northridge, CA 91330